# Doktorska disertacija

By: Jelena Mijuskovic

As of: Feb 2, 2022 7:18:28 PM 30.793 words - 412 matches - 213 sources Similarity Index

19%

Mode:	Similarity Report V	
paper te	rt:	

UNIVERSITY OF MONTENEGRO FACULTY OF SCIENCE AND MATHEMATICS AND UNIVERSITY PARIS SACLAY Jelena Mijušković MEASUREMENT OF N-JETTINESS VARIABLES IN THE PRODUCTION OF Z BOSON EVENTS WITH THE CMS DETECTOR AND PERFORMANCE OF ITS ELECTROMAGNETIC CALORIMETER - Doctoral thesis - 2022 Abstract

This thesis presents the measurements of differential cross section of Z boson production
in association with jets in proton-proton collisions at center of mass energy of 13 TeV. The
analysed data has been collected by the CMS experiment of LHC during the year 2018 and
corresponds to an integrated luminosity of 59 fb-1. The

cross sec- tion is measured as a function of track-based event shape variables: zero-jettiness, one-jettiness and sum of the transverse momentum of particles, and jet-based event shape variables:  $\tau$ sum and  $\tau$ max. The measurements of event shape variables are performed for the events where pairs of muons are produced in

the decay of a real Z boson with an invariant mass between 76 and 106 GeV

. Track-based varibales are also measured for off shell Z bosons with an invariant mass between 125 and 150 GeV, 150 to 350 GeV and 350 and 1500 GeV and in four different Z boson transverse momentum regions. The measurements

have been compared with three types of theoretical predictions with LO, NLO and NNLO 3

QCD accuracies obtained with two MC generators , Mad-Graph5\_ amc

@nlo and Geneva. Part of the thesis is devoted to the studies of the performance and intercalibra-tion of Electromagnetic calorimeter (ECAL) during Run 2 data taking period (2016, 2017 and 2018). This subtedector is crucial for detection of photons and electrons, therefore it is very important for many searches at CMS. With the constant monitoring and calibration excellent performance was obtained. The resolution during Run 2

the performance from Run 2 is very close to the one from Run1 despite

4

ageing of the detector and much higher instantaneous luminosity. Sažetak U ovom radu prikazano je mjerenje diferencijalnog presjeka za kreaciju Z bozona i džetova nastalih pri proton-proton sudarima na energiji od 13 TeV. Događaji koji se analiziraju detektovani su u CMS eksperimentu na LHC-u tokom 2018. godine. Luminoznost podataka iznosi 59 fb-1. Diferencijalni presjek je mjeren u funkciji od variabli zasnovanih na česticama: 0-džetnost, 1-džetnost i suma transverzalnih impulsa naelektrisanih čestica, kao i u funkciju od varijabli zasnovanih na džetovima: tsum and rmax. Diferencijalni presjek je mjeren u događajima sa dimionskim parovima nastalih pri raspadu Z bozona sa invarijantnom masom u opsegu od 76 do 106 GeV. Varijable zanovane na česticama su takođe mjerene u oblasti sa kreacijom virtuelnog Z bozona, sa invarijatnom masom od 125 do 150 GeV, od 150 do 350 GeV i od 350 do 1500 GeV, kao i u oblastima sa različitim transverzalnim impuslom Z bozona. Mjerenja su upoređena sa teorijskim predviđanjima sa različitim stepenom preciznosti, dobijenih sa dva Monte Karlo generatora, MadGraph5\_amc@nlo i Geneva. Dio teze je posvećen interkalibraciji i performansama Elektromagnetnog kalorime- tra (ECAL) tokom tzv. Run 2 perioda prikupljanja podataka (2016, 2017 i 2018 godina). U ovom detektoru vrši se detekcija fotona i elektrona, što ga čini veoma važnom komponentnom za veliki broj analiza koje se odvijaju u CMS-u. Sa kon- stantnom kalibracijom i monitoringom, odlične performance ECAL-a su postignute tokom Run 2 perioda. Dobijena rezolucija je na nivou 1.7 % u centralnoj oblasti detektora. Takođe je pokazano da su perfromase detektora tokom Run 2 perioda približne performansama sa početa rada samog detektora (Run 1), uprkos starenju detektora i mnogo većoj luminoznosti. Résumé (Section à remplir)

Contents List of Figures 8 List of Tables 14 Introduction 15 1 Theory overview 201

1.1 5	tandard Model		17	<b>1.1.1 The</b> into	eractions in	55
Stand	ard Model	18 <b>1.1.2</b>	Beyond Sta	ndard Model		
25 <b>1</b>						
			06.1.2 Drall	Van muaaaa		
roton - pi	oton collisions		. 26 1.3 Dreii -	ran process		
	nte Carlo Simulation		30 1.	4.1 MadGran	h5 amc@nlo	3
4 Moi						

Experimental setup 34 2.1 Large Hadron Collider
of the Large Hadron Collider
<b>2.1.2 Performance of LHC</b>
Compact Muon Solenoid
2.2.1 Coordinate system       41 2.2.2 Superconducting solenoid       7         42 2.2.3 Tracker       43 2.2 .4 The         electromagnetic calorimeter       46 2.2 .5 The hadronic calorimeter         47 2.2 .6 Muon system       49 2.2 .7 Trigger
51
2.3 Physics object reconstruction
Calorimeter clustering
3 ECAL Calibration 57 3.1 Energy reconstruction

	k
4 Monte Carlo corrections	87 4.4.2
Rochester	. 87 4.4.4
Trigger Scale factors	91 4.5 4.6
Unfolding method	. 99 4.6.1
heoretical predictions uncertainties	102 5
Measurement of jet-based event shape observables 122 5.1 Observable definition	122
5.2 Jet reconstruction and selection	
128 5.4 Results	
List of Figures 1.1 Overview of the fundamental particles of the Standard model [5]	155
radronization process	ess
Sketch of proton-proton collision as simulated by a Monte Carlo event generator	96
ellow[37]	5 2.3 Schemati 8] 38
ellow[37]	5 2.3 Schemati 8] 38 ions [44]
ellow[37]	5 2.3 Schemati 8] 38 ions [44] d transverse
ellow[37]	5 2.3 Schemation 38 ions [44]
27]	5 2.3 Schemation 38 ions [44]d transverse ight part

HCAL detector 48 2.15 Schematic view of the longitudinal layout of the muon detector system. 50 2.16 A
flowchart of the L1 trigger
signature in the subdetectors
1 Example of fitted pulses for simulated events with 20 average pileup interactions and 25 ns bunch spacing, for a signal in the barrel (left) and endcap (right
)
Relative response to laser light (440 nm in 2011 and 447 nm from 2012 onwards) injected in the  ECAL crystals, measured by the ECAL laser monitoring system, averaged over all crystals in bins of pseudo- rapidity. The bottom plot shows the instantaneous LHC luminosity delivered during this time period
stability of the relative energy scale measured from the invariant mass distribution of $\pi0\rightarrow\gamma\gamma$ [51] decays in
EB and plotted
as a function of time, over a period of 3 hours
during an LHC fill
ratio of scale parameters between data and simulation, in gray for
R9 >0.94 electrons and in green for R9 < 0.94 electrons 68 3.6 Map of the intercalibration constants for ECAL
barrel region 69 3.7 Corrections applied to account for the effect of gaps between the supermodules
70 3.8 Final map of the final intercalibration constants for barrel and end- caps for 2018
71 3.9 Overall precision of the different IC measurement methods as well as their combination

for 2016 (top left), 2017 (top right), and 2018 (bottom	12
) 72 3.10	
Energy resolution as a function of the pseudorapidity for the 2018 dataset with the	151
preliminary and refined calibration	
Energy resolution with the refined calibration as a function of the pseudorapidity comparing	4
2016, 2017, and 2018 data-taking periods (left) and Run 2 with 2012 data-taking	4
(right)73 3.12 Contribution to the ECAL energy resolution from different effects on the (legical cumulative energy resolution obtained by adding up the contribution from different effects	74
Energy resolution (left) and time resolution (right) obtained in the test beam campaign with the CATIA ASIC connected to a commercial ADC	4
[74]	al, and all on matched and simula- tion
invariant mass distribution with linear(left) and logarithmic (right) scale	54

bution of zero-jettiness computed for the 4.17 Data to simulation comparison and the
function of zero-jettiness for 12 < pT (Z ) < 25 ial cross section as a function of zero-omparison and the differential cross section 2 Data to simulation comparison and the GeV
function of zero-jettiness for 12 < pT (Z ) < 25 ial cross section as a function of zero-omparison and the differential cross section 2 Data to simulation comparison and the GeV
ial cross section as a function of zero- comparison and the differential cross section  2 Data to simulation comparison and the  3 GeV
omparison and the differential cross section  2 Data to simulation comparison and the  3 GeV
2 Data to simulation comparison and the GeV
GeV
ss for 350 < MII < 1500 GeV
function of one-jettiness
a agostian as a function of one intrinces for Co
s section as a function of one-jettiness for 6 <
I the differential cross section as a function of
ation comparison and the differential cross
. 112 4.28 Data to simulation comparison and
GeV
one-jettiness for 125 < MII < 150 GeV
ion as a function of one-jettiness for 150 < MII
ifferential cross section as a function of one-
comparison and
transverse momentum of 34
verse momentum of charged 5

differential cross section as a function of the sum of the transverse momentum of

charged particles 6 <pt(z)<12gev116 4.35="" and="" comparison="" data="" simulation="" th="" the<="" to=""></pt(z)<12gev116>
differential cross section as a function of the sum of the transverse momentum of charged particles for 12 < pT ( Z
) < 25 GeV
differential cross section as a function of the sum of the transverse momentum of charged 5 particles for pT ( Z
) > 25 GeV
differential cross section as a function of the sum of the transverse momentum of charged 5 particles for
125 < MII < 150 GeV
differential cross section as a function of the sum of the transverse momentum of charged 5 particles for
150 < MII < 350 GeV
differential cross section as a function of the sum of the transverse momentum of charged 5 particles for
350 < MII < 1500 GeV
4 Data to simulation comparison of the leading jet transverse momen- tum

and inclusive number of jets
$\dots$ 129 5.6 Data to simulation comparison and the differential cross section as a function of $\tau$ max $\dots$
$\dots$ 130 . 5.7 Data to simulation comparison and the differential cross section as a function of $\tau$ sum $\dots$
131 . List of Tables 4.1 List of data samples
used in the analysis
and their cross section. 82 4.3 Medium ID criteria used for muon selection 83 4.4 PV association flags
description
The Standard Model Theory, developed in 1960s, describes the elementary particles and interactions between them.
Since its proposal, enormous work has been done to experimentally verify the predictions of this theory. The results
obtained from many high energy physics experiments such as Tevatron at Fermilab (1983 to 2011), the Large Electron
Positron Collider at CERN (1989 to 2000), the Hadron Electron
Ring Accelerator at DESY (1992 to 2007) and the Large Hadron Collider at CERN (from 2010 ) and the Large Hadron Collider at CERN (from 2010 ) have shown a good agreement of the measurements with the theoretical predictions
. However, this is not a complete theory and there are still unanswered questions that different theories beyond Standard
Model attempt to be explain. In 2012 the existence of Higgs boson was confirmed at the LHC by CMS [1] and ATLAS [2] experiment. It
was the last missing piece of Standard Model . The LHC experiments 213
continued their work with studies of the properties of the Higgs boson, high precision measurements of well known processes and with
searches for new physics beyond Standard Model . The processes of interest are identified by

looking for signal with specific numbers of leptons, photons or jets. To discriminate the signal from the background events, it is often needed to use veto on the hadronic activity in an event. This veto is typically based on jets but could also be implemented using track based event shape variables such as N-jettiness [3] or jet-based event shape variables [4]. One of the advantages of using inclusive event shape variables is that the

## summation of logarithms to next-to-next-to-leading logarithmic order

178

75

can be performed. From experimental point of view, the event shape variables provide efficient method to veto jets.

Using the jet based variables, the central jets can be vetoed while the phase space constrains are not strict. Before using these variables in analyses, it is essential to ensure that they are well described with the Monte Carlo simulatios, which can be done by comparing the predictions with measurements. The research presented in this thesis are measurements of track-based and jet-based event shape observables in events with one Z boson produced at LHC

in proton-proton collisions at center of mass energy of 13 TeV . The measurements are done using the data collected in 2018 by the CMS detector. The

measurements of track-based event shape varibles are performed for events where pairs of muons are produced in the decay of a real Z boson with an invariant mass between 76 and 106 GeV, and also for off shell Z bosons with an invariant mass between 125 and 150 GeV, 150 to 350 GeV and 350 and 1500 GeV. In addition, these variables are measured in four different Z boson transverse momentum regions. Part of this thesis is devoted to the intercalibration of the Electromagnetic Calorime- ter (ECAL) of CMS. This subdetector is crucial for the detection of photons and electrons and its calibration is very important for many searches performed with CMS. This thesis is organized as follow. The theoretical introduction to the

## Standard Model is described in chapter 2. In chapter 3, the

101

experimental setup is presented. Intercalibration and performance of ECAL is described in chapter 4. The measurements of track-based event shape variables are presented in chapter 5, and the measurements of jet-based event shape variables are presented in chapter 6. Sum-mary and confusions follows. Chapter 1 Theory overview 1.1

Standard Model The Standard Model of particle physics (SM) is the theory developed in 158 the 1960s that describes the

### fundamental particles

and the interactions between them . This theory models the electromagnetic, weak, and strong interactions using the

Quantum Field Theory (QFT) formulation. The gravitational force, which is negligible at the subatomic level, is not included in the

SM. According to the SM, all matter is made of particles with spin

183

1 called fermions, 2 and the interactions between them are mediated by particles with integer spin called bosons (Figure 1.1).

Fermions can be classified into two groups: leptons and quarks . Each of the

99

twelve fermions has its corresponding antiparticle. Leptons are particles that interact via the electromagnetic and weak interactions. Their charge is integer or null. The

charged leptons are electron (e), muon ( $\mu$ ), and tau ( $\tau$  ). The corresponding neutral

175

leptons, which interact only through the weak interaction,

are the electron neutrino (ve), the muon neutrino (v $\mu$ ) and the tau neutrino (v $\tau$ ). Quarks

157

interact through the electromagnetic, weak, and strong interactions. The electric charge of quarks is fractional and it is 2 for the up (u), charm (c) and top 3 (t) quarks and -1 for the down (d), strange (s) and bottom (b) quarks. The quarks 3 do not exist as a free state but they form bound states called hadrons. The hadrons Figure

#### 1.1: Overview of the fundamental particles of the Standard model

56

[5]. composed by three quarks (antiquarks) are called baryons (antibaryons) while the bound states formed by quarkantiquark pair are called mesons. The charge of hadrons is null or integer. The fermions

are divided into three generations . The fermions from the first generation, which are the

123

lightest ones, make the ordinary matter. The second and third generation paricles, except neutrinos, are unstable and are accessible at higher energies. Bosons, with spin 1,

are the mediators of the electromagnetic , weak, and strong interaction. The photon (γ) 61 is massless and is the mediator of electromagnetic interaction , while the W± and Z bosons are massive and 69 the mediators of the weak interaction. The strong force is carried by massless are gluons (g ). In addition to the spin-1 **bosons, there is** a **Higgs boson** with the **spin-0** , mediator of 13 the scalar Higgs field. It was discovered in 2012 by the CMS and ATLAS collaboration [1, 2]. 1.1.1 The interactions in Standard Model The SM is a gauge theory based on the  $SU(3)C \times SU(2)L \times U(1)Y$  symmetry, where the strong 140 interaction is associated to the SU(3)C symmetry and  $SU(2)L \times U(1)Y$  is the symmetry group for the electromagnetic and weak interaction 90 . Quantum electrodynamics Quantum electrodynamics (QED) is the theory that describes the electromagnetic interaction 103 . To deliver the QED Lagrangian, we start with the Dirac Lagrangian [6] that describes the motion of the free fermion in each point of space-time x: LDirac =  $\psi(x)(i\gamma\mu\delta\mu - m)\psi(x)$ , (1.1)

98

where  $\gamma$  are Dirac matrices and  $\psi(x)$  fermionic field

. This Lagrangian must be invariant under the gauge transformation of the field

$$\psi(x): \psi(x) \rightarrow \psi'(x \quad) = eie\alpha(x) \quad \psi(x), \ (1 \quad .2) \quad \text{where} \quad \alpha(\quad x \quad) \ \text{is} \quad \text{any} \quad \text{function} \quad \text{of} \quad x \quad \boxed{53}$$
 and  $e$  is

the dimensionless coupling strength of electrodynamics. In order to achieve invariance, the derivative  $\delta\mu$  must be replaced with the covaraint derivative :  $\delta\mu\to D\mu=\delta\mu+ieA\mu$ , (1.3) where  $A\mu$  is the gauge field that corresponds to the photon and has the transforma- tion property:  $A\mu\to A'\mu=A\mu-\delta\mu\alpha(x)$ . (1.4) To complete the QED Lagrangian, the kinematic term describing the propagation of photons needs to be included. This is done by introducing the field strength F  $\mu\nu$  defined as: F $\mu\nu=\delta\mu A\nu-\delta\nu A\mu$ , (1.5) which leads to the photon propagation term : Lgauge = -1 F  $\mu\nu$  F $\mu\nu$  . 4 (1.6) The final Lagrangian of the QED

can be written as : LQED = 
$$\psi(x)(i\gamma\mu\delta\mu - m)$$
  $\psi(x) - e(\psi(x))$ 

))γμ $\psi$ (x))Αμ – 1FμνFμν. 4 (1.7) The first term of Lagrangian corresponds to the

free propagation of fermions, the second term represents the interactions of fermions defined and photons, and the last term takes into account the propagation of

photons. Quantum chromodynamics The strong

interaction is described by the Quantum Chromodynamics (QCD ) theory which is based on 64 the gauge symmetry group SU(3). The

particles that interact with the strong force (quarks and gluons) have

an additional quantum number called color. The quarks can have one of the three colors: red , blue or green

, while the antiquarks have anticolors. The eight gluons are carrying the combination of color and anticolor: rb, rg, br, bg, gr, gb, 12 (rr gg) and  $\sqrt{1}$  (rr bb – 2bb). – 6 + Following the procedure for QED described in the previous section, the staring point for QCD is also the Dirac Lagrangian defined in Eq. 1.1 . The interaction is introduced by requiring the Lagrangian

to be invariant under the following gauge transformation:  $\psi(x) \rightarrow \psi$  '(x) =  $U\psi(x)$ 

88

) = (eig  $a\theta a(x)Ta)\psi(x)$ , (1.8)  $\sum$  where g

is the dimensionless coupling strength of the strong force and Ta are the eight generators of SU(3

) symmetry related with Gell-Mann matrices as Ta =  $\lambda a/2$ . To make the Lagrangian invariant under this transformation, similarly to QED, a covariant derivative is introduced:  $D\mu = \delta\mu + igTaG\mu bGvc$ , (1.9) where  $G\mu$ a are eight gauge fields (a = 1,..8). The gauge transformation properties of the gauge fields are defined as:  $G\mu b \rightarrow G'b\mu = G\mu b - \delta\mu\theta b - g\lambda abc\theta aG\mu c$ . (1.10) where  $\theta$  being eight functions of space-time coordinates. The field strength can be written as:  $Fa\mu\nu = (\delta\mu Gva) - (\delta\nu G\mu a) - g\lambda abc G\mu bGvc$ . (1.11) Therefore, the QCD Lagrangian has the form:  $LQCD = \psi(i\gamma\mu\delta\mu - m)\psi - g(\psi\gamma\mu Ta\psi)G\mu a - 1(\delta\mu Gva - \delta\nu G\mu a)(\delta\mu Gav - \delta\nu Ga\mu) + 12g\lambda abc G\mu bGvc(\delta\mu Gav - \delta\nu Ga\mu) - 14g2\lambda abc\lambda ars G\mu bGvc Gr\mu Gsv$ . 4 (1.12) In this Lagrangian, the first term describes free quark propagation. The second term represents the quark-gluon interaction. Gluon propagation term corresponds to the third term. The last two terms are the triple coupling and the quadrupole coupling, which introduce the gluons interaction with themselves. The fact that the quarks

do not exist as free particles and can only be detected in bound states

91

, can be explained by gluon-gluon interactions. If we consider two quarks pulled at some distance, the exchange of gluons and the interaction between the gluons themselves would squeeze the field and increase the force. Since the field becomes proportional to the distance between quarks, an infinite amount of energy would be needed to separate them at infinity. Therefore, the

quarks cannot be detected as free particles, but only in bound colorless states . 190
This property of

strong interaction is called color confinement. The consequence of the color confinement is the process of hadronization. As shown in Figure 1.2, the quark-antiquark pairs are separated and the energy of the color field between them increases as they are moving apart from each other. When this energy becomes high enough,

a new quark -antiquark pair is produced. This process is repeated until the quarks have

low enough energy to create hadrons. The produced hadrons are often the results of boosted interactions, which makes the particles to be collinear and from what is called a jet. Figure 1.2: Schematic view of hadronization process.

Another important property of QCD is the asymptotic freedom which describes the quarks 163 at the high energy

regime. With the high energies, the coupling,  $\alpha s = g2/4\pi$ , decreases which means the interaction between quarks and gluons becomes weaker. For the very

high energies, the quarks and gluons can be considered as free , non-interacting particles

and are refered to as partons. Electroweak interaction The electroweak theory, proposed

by Glashow, Weinberg, and Salam [7, 8, 9], is the theory that unites the electromagnetic and weak interaction

. The electroweak interaction follows SU(2)L × U(1)Y symmetry, which requires three fields

for SU(2)L : W1, W2, W3 and one field for U(1)Y : B. The

generators

are the weak isospin T ad the weak hypercharge Y . Their relation to the electric 83 charge is

16

52

: Q = T3 + Y 2 . (1.13) In the electroweak theory, it has to be taken into account that the right and the left projections of the fields do not behave the same. They are defined by the chirality operators PR,L :  $\psi$ R,L = PR,L $\psi$  = 2 1(1 ±  $\gamma$ 5) $\psi$ . (1.14) The fermions that are associated with the left projection of the field (

left-handed fermions ) are doublets, while the right-handed fermions are isospin singlets

.  $\psi$ L = veL ( eL ) (1.15)  $\psi$ R = (veR), (eR). As in the case of QED and QCD, the gauge transformation is introduced and the invariance under this transformation is required by introducing the covariant deriva- tive:  $D\mu = \delta\mu + igTkWk\mu + ig2' Y B\mu$ . The interaction term in Lagrangian has the form: LEinWterKaction = -g' 2 ( $\psi\gamma\mu Y \psi$ )B $\mu - g(\psi T kY \psi)W k\mu$ . 22 (1.16) (1.17) The gauge bosons W±, Z and γ cannot be directly determined from the gauge fields. By intorducing the rotation angle θW (the Weinberg angle) the electroweak interaction Lagrangian can be expressed in terms of the gauge bosons:  $B = A\cos\theta W - Z \sin\theta W W 3 = A\cos\theta W + Z \sin\theta W W 1,2 = W - \pm W + \sqrt{2}$ . The rotation angle is defined by the coupling strengths:  $e=g\sin\theta W = g'\cos\theta W$ . Finally, the interaction term of Lagrangian can be expressed as: LEinWterKaction =  $-\sqrt{g}$  (veLγμW-eL + eLγμW+vL)  $-e\psi\gamma\mu AQ\psi - 22\sin\theta W\cos\theta W \psi\gamma\mu Z[T3 - 2Q\sin\theta W2 - TL3γ5]\psi$ . e (1.18) (1.19) (1.20) The first term in the equation corresponds to the weak interaction with the change of electric charge mediated by W± bosons. They interact only with left-handed fermions. The second term represents the photon-fermion interaction, which was present in the QED Lagrangian (Eq. 1.7). The last term is the neutral

weak interaction mediated by the Z boson . This interaction does not distinguish left-

and right-handed fermions. Electroweak symmetry breaking The mass terms are added in Lagrangian 1.20 with the Brout-Englert-Higgs mech- anism [10, 11] that breaks spontaneously the gauge invariance symmetry. The following terms are added: LHiggs =  $(D\mu\phi)\dagger(D\mu\phi)$  – V  $(\phi)$ , (1.21) where  $\phi$  is a complex scalar field while the V( $\phi$ ) is the potential of the field. In order to include the mass term, this field needs to have at least three degrees of freedom:  $\phi$  = ( $\phi$ 0 =  $\sqrt{2}$  ( $\phi$ 3 +  $i\phi$ 4)  $\phi$ + 1  $\phi$ 1 +  $i\phi$ 2. (1.22)) The

potential of the field , called Higgs potential, is defined as:  $V(\phi) = \lambda(\phi + \phi) = \lambda(\phi + \phi) = \lambda(\phi + \phi)$ 

. (1.23) If the  $\lambda$  term and  $\mu$ 2 are positive, the potential is also positive with the single minimum at  $\phi$  = 0. In the case of  $\mu$ 2 < 0 and  $\lambda$  > 0, the potential has an infinite set of minima at:  $\phi+\phi$  = 1( $\phi$ 21+ $\phi$ 22+ $\phi$ 23+ $\phi$ 24)=- $\mu$ 2 $\lambda$ 2 = 1 $\nu$ 2. 2 2 (1.24) In the second case, the spontaneously symmetry breaking can be achieved. The ground state is typically chosen as :  $\phi$ 0 =  $\sqrt{1}$ 0 2 ()  $\nu$  . (1.25) The

**Lagrangian is invariant under the symmetry** transformation **but the** potential around **the** minimum is not. **The** 

shape of potential is graphically

ground state, the Higgs Lagrangian can be written as : LHiggs = 12 δμhδμh - 80 12ν2λh2 2

masses of the gauge bosons are measured experimentally with great precision, and their values are

MW = 80.379 GeV [13] and MZ = 91.1876 GeV [14]. The experimentally measured mass of Higgs boson is MH = 125 GeV [1] [2]. 1.1.2 Beyond Standard Model The Standard Model theory is so far consistent with all the experimental results, however, there are still open questions that are not addressed by this theory. Some of the shortcomings of the SM are: • dark matter and dark energy: according to the present results the 5 % of the

Universe is made of ordinary matter, about 25 % of dark matter while the rest is dark energy

[15]; the particles that are defined by Standard Model are excluded as the particles that compose dark matter, therefore an extension of SM is needed; • asymmetry between matter and antimatter: the asymmetry in presence of

matter and antimatter in the Universe is not explained by the SM

14

; in order to provide an explanation, new theories need to be developed; • neutrino masses: the observations of the neutrino mixing confirmed that the neutrinos are particles that have mass; according to the SSB mechanism, the neutrinos do not acquire mass, therefore it is needed to have the extension of SM which would explain this effect; • gravity: the gravitational interaction is not included in SM; the effects due to the gravity are negligible at the accessible energy scale and it becomes relevant at the scale higher than the TeV scale; however, there are attempts to include gravity into the SM with a spin-2 mediator graviton. 1.2 Proton - proton collisions Protons are baryons composed of two u quarks and one d quark. These quarks, called "valence" quarks, interact

with each other whitin the proton and exchange gluons, which also can interact with

23

themselves and

produce more gluons or quark- antiquark pairs called "sea" quarks. The

150

quarks and gluons from protons are referred to as partons. According to the parton model [16], the partons carry the fraction of the total proton momentum and are

described by parton distribution function (PDF), which gives the probability

110

that parton has

a fraction x of the total proton momentum P (pi = xP). The cross section of proton - proton

73

interaction cannot be computed easily, due to the complex structure of protons. Using the collinear factorisation [17], the cross section for the interactions of two protons with the final state X (pp  $\to$  X), can be written as:  $\sigma pp \to X = dxadxbfa(xa, \mu F)fb(xb, \mu F)\sigma ab \to X (xaxb, \mu R, \mu F) (1.29) \sum a,b \int$ , where the sum runs over all the flavours of partons and  $\sigma ab \to X(xa,xb,\mu R,\mu F)$ 

is the cross section at the partonic level. The partonic cross section depends on the

18

energy of partons (xa, xb) and the scale  $\mu$ F at which the factorization is performed. Since the calculations are performed with a pertubative expansion in  $\alpha$ ns that keeps only the first terms, the

cross section depends on the renormalization scale µR as well. The

193

PDFs are obtained mainly from the deep inelastic scattering (DIS) exper- iments such as lepton-hadron collider HERA [18] [19], hadron colliders, such as LHC, and from the fixed target experiments. The PDFs

depend on the scale at which the hadron is probed

evolution of PDFs with the scale  $\mu F$ . This evolution is described by the

146

Dokshitzer-Gribov- Lipatov-Altarelli-Parisi (DGLAP) equations [20, 21, 22]:  $\delta fa(x, \mu F) \mu F = \alpha s(\mu 2F) 1 d\xi \delta \mu 2F 2\pi Pa \rightarrow bc($ ,  $\mu F) fa(\xi, \mu F)$ ,  $x \xi (1.30) \int x \xi$  where  $Pa \rightarrow bc$  is the Atarelli-Parisi splitting function, that gives the probability for  $\sum a$  parton a to split into two partons bc. The resulting particle has a momentum fraction  $\xi$  of quark momentum pa. The produced parton c is absorbed by the proton sea quarks. Because of the universality of the PDFs, it is possible to use PDFs extracted from well-known processes for the predictions with different scales or different final states. The modern PDF sets, which are available through the LHAPDF library [23], include data from several experiments and in several different final states. In Figure 1.4 the NNPDF3.1 PDF is shown. Figure 1.4: The scale dependence of the NNPDF3.1 set of PDFs [24]. 1.3 Drell - Yan process The process of creation of lepton pairs from the hadron collision was proposed

by Sidney Drell and Tung-Mow Yan in 1970 [25] for testing the

62

parton model. This process, named Drell-Yan after them, consists of the annihilation of quark-antiquark pairs from hadrons with the creation of

**Z** boson or virtual photon, which decays into lepton-antilepton pair . The Feynman diagram of

28

this process is shown in Figure 1 .5. Figure 1 .5: Feynman diagram of Drell-Yan process. The

66

cross section for the Drell-Yan process, following the Eq 1.30, can be written as:  $\sigma(pp \to l+l-) = dxqdxqfq(xq,\mu2F)fq(xq,\mu2F)\sigma(qq \to l+l-)$ , (1.31)  $\Sigma q \int \int where the \sigma(qq \to l+l-)$  is the

cross section of the lepton-antilepton production by a quark-antiquark pair. The

87

renormalization and factorization scale for the Drell- Yan process is usually chosen to be equal to the invariant mass of leptons ( $\mu$ 2F =  $\mu$ R2 = MZ2). Following the perturbative QCD, the

partonic cross section can be expanded in series with respect to the coupling constant 169 αs: σ

 $(qq \rightarrow l+l-) = \sigma LO + \alpha s \sigma NLO + ... (1.32)$  The partonic cross section can be calculated using the Matrix Element of the Feynman diagram. For the leading order (LO), on the Feynman diagram it can be seen that there are no strong interactions. For higher orders, the gluons can be emitted from the quarks. In Figure 1.6 examples of

LO and next-to-leading order (NLO ) diagrams are shown . When performing calculations for

higher order diagrams, loops of quarks and gluons must be included. With these additional terms the logarithms of the form ( $\alpha \log Q2/M$  2)n where is the number of quark (gluon) loops and M the renormal- n ization point of  $\alpha s$ , are introduced. The current best computation available are at the NNLO.

$$\mathbf{q} \mathbf{Z}/\mathbf{\gamma} * \mathbf{l} + \mathbf{q} \mathbf{Z}/\mathbf{\gamma} * \mathbf{l} + \mathbf{q} \mathbf{l} - \mathbf{q} \mathbf{Z}/\mathbf{\gamma} * \mathbf{l} + \mathbf{q} \mathbf{q} \mathbf{l} - \mathbf{g}$$
 38

q Figure 1.6: Drell-Yan process at LO (a), at NLO with an initial state radiation (b), at NLO with a gluon loop at the initial state (c), and at NLO with a quark-gluon initial state and with an outgoing hadronization. Besides of the hard scattering, the process that involves large momentum transfer between the colliding particles, several different effects can occur in

proton-proton collisions. The part of the energy of the partons from the

hard interaction can go to the radiation of gluons and photons. Radiated gluons and photons can create additional quarks and lepton pairs. Since gluons are particles that can self-interact, they can produce additional gluons or quark-antiquark. Such radiation created from partons is called parton shower. The radiation coming from the initial state particles is called initial state radiation (ISR), similarly the radiation from final state particles is called final state radiation (FSR). Colored particles created in shower combined themselves to create hadrons is explained in Section 1.1.1. At the high energy proton-proton collisions, there are also additional soft inter-actions coming from the remaining partons of protons. These secondary interactions are called underlying events. The underlying events is common name for multiple parton interaction (MPI) and beam remnant (BBR) interactions. The particles that are produced in the underlying events usually have low transverse momentum. 1.4 Monte Carlo Simulation The simulations that includes physics processes and also the response of the detector have very important role for the measurements and discovery. In order to compare what is measured in the experiment with the theoretical prediction, it is needed to simulate the proton-proton interactions, the

interaction of the produced particles with the detector and the response of the

15

detector including its electronic.

To simulate the processes from the proton-proton collisions, which implies the computation of large intergals, the

209

Monte Carlo (MC) technique is used [26]. To describe the

typical high energy event, event generator should include simulation of several physics

48

effects that are schematicly shown in Figure 1.7 The simulation of the proton-proton event

is performed in the following steps: The evolution of an event in simulation

152

starts with the two beam particles that are going towards each other. The initial particles are generated according to the set of PDF which provides the information about partonic substructure. • The partons from beams starts start with the radiation and initial state shower is simulated. • The incoming partons (one from each beam) enters the hard interaction and the outgoing partons are produced. In this step, according to the nature of the hard interaction the main characteristics of event are determined. • In the hard proces the short-lived resonances can be created and their decay is considered in this step. • The outgoing partons undergo radiation and final state radiation is simulated. • The simulation of underlying events. Figure 1.7:

Sketch of proton-proton collision as simulated by a Monte Carlo event generator [27] . •

96

The

process of hadronization is simulated. • The

decay of long -life particles, such as  $\tau$  leptons or B- hadrons

software [28]. The geometry of the CMS experiment is implemented in the software, as well as the information about the active and inactive volume. The signal created by the particles as they go through the detector is simulated and it is reconstructed using the same algorithm used for data. The signal samples that are used for this analysis are simulated using Mad-Graph and Geneva MC generators. In both cases the initial and final state parton shower and hadronization Pythia8 [29] is used. 1.

4.1 MadGraph5\_amc@nlo MadGraph5\_amc@nlo [30] is a

3

framework to compute cross sections and generate parton-level events that can be showered with a MC generator like pythia8 or Herwig. It computes automatically LO and NLO cross sections and provides the tools to the PS simulations. It generates automatically the Feynman diagram up to NLO and also computes automatically the loop contributions. In this thesis,

two different predictions from MadGraph5\_amc@nlo 3 are used: • MadGraph5\_amc@nlo including ME computed at LO for up to 4 partons . The interface with pythia8 is done using the kT **MLM scheme** [31]; • MadGraph5\_amc@nlo including ME at NLO for up to 2 partons . The interface with pythia8 is done using FxFx merging scheme

[29]. Both of these predictions are interfaced with pythia8 for the parton showering. The effect of underlying events in the simulation is modelled using pythia8 with specific parameter called tune. For the mentioned samples, the CP5 tune of pythia8 [32] is used. 1.4.2 Geneva Geneva [33, 34] is a MC generator for Drell-Yan processes that matches analytic resummation to an NNLO fixed order prediction. The NNLL' resummation of the global event shape variable N-jettiness ( $\tau$ N) is used [3]. The  $\tau$ N will be described in more detail in Sec. 4. For computing the cross section, the phase space is divided using the variable  $\tau$ N, and the zero, one and two jets spaces can be distinguished:  $\theta$ 0events:  $\theta$ 0MC( $\theta$ 0C( $\theta$ 0Cut),  $\theta$ 0  $\theta$ 1events:  $\theta$ 1 do $\theta$ 1M1C ( $\theta$ 1 >  $\theta$ 1Cut;  $\theta$ 1) (1.33)  $\theta$ 2events:  $\theta$ 3 do $\theta$ 4M2C ( $\theta$ 2 >  $\theta$ 3 cut;  $\theta$ 4 >  $\theta$ 5 cocut and  $\theta$ 5 and  $\theta$ 5 the resolution cut  $\theta$ 5 cocut, similarly the 1-jet case is defined by  $\theta$ 5 >  $\theta$ 7 cut and  $\theta$ 7 >  $\theta$ 8 cocut and  $\theta$ 7 >  $\theta$ 9 cut and  $\theta$ 7 >  $\theta$ 9 cut and  $\theta$ 7 >  $\theta$ 9 cut and  $\theta$ 8 cocut and  $\theta$ 9 cocut and

cross section for some observable X can be written as:  $\sigma(X)$ 

198

) =  $d\Phi 0 \ d\sigma 0 \ MX(\Phi 0) + d\Phi 1 \ d\sigma 1 \ MX(\Phi 1) + d\Phi 2 \ d\sigma 2 \ MX(\Phi 2)$ ,  $(1.34) \int d\Phi 0 \int d\Phi 1 \int d\Phi 2$  where  $MX(\Phi N)$  is the mesurements function for computing X for the N-parton final state  $\Phi N$ . In this thesis, the Geneva with  $\tau 0$  resummation is used. The PDF set used is PDF4LHC15 and  $\alpha s(mZ)$  is set to 0.118. Showering is done using a modified version of Pythia (version

8.235). The underlying events are modeled with the the CUETP8M1 [35] tune of Pythia8. Chapter 2 Experimental setup The analysis presented in this thesis is done by with data obtained

from proton- proton collisions it the center of mass energy of 13 TeV . Protons are accelerated in the

Large Hadron Collider (LHC) and the particles are detected with the Compact Muon

Solenoid

(CMS). CMS is a very complex detector that contains several differ- ent subdetectors systems. By combining the information from the subsystems, the complete picture of one collision is obtained: the produced particles are identified and their momentum at the interaction point is measured. In this chapter, the accelerator system and the detector with its subsystems are presented. In section 2.1 a brief description of LHC, its performance and future plans are presented. Section 2.2 is devoted to the CMS experiment. The reconstruction of particles inside of the detector is described in section 2.3.

2.1 Large Hadron Collider The Large Hadron Collider [36] is a circular accelerator

designed to collide protons or heavy ions . It is the

largest and most powerful accelerator ever built. The circumference of the LHC is 27 km and the accelerator is located at the French - Switzerland border, close to Geneva (Figure 2.1), at an undeground depth between 45 and 175 m. The

collider is placed in a circular tunnel built for the Large Proton Electron collider (LEP 96

) which was operating until the year 2000 and had an essential role in studies of the Z and W bosons properties. Figure 2.1: Aerial view of Geneva region, with the position of LHC sketched in yellow [37]. The LHC was proposed in 1994 by the European Organization for Nuclear Re- search (CERN), while the first results with this machine were obtained in 2010.

One of the main goals of the LHC was the search for the Higgs boson, which was 85

discovered by the CMS and ATLAS detectors in 2012 [1, 2]. After the discovery, the operations continued with performing a number of precision measurements

6 to study the properties of the Higgs boson . In addition, energies reached by the collisions it is possible to perform searches for new physics beyond by Standard Model. 2.1.1 The design of the Large Hadron Collider The LHC is designed to study proton-proton collisions that can 76 reach the center of mass energy of 14 TeV and heavy ion the center of mass energy of up to 2.76 TeV In order to collisions at per nucleon. 67 achieve the design energy, before entering the LHC ring, beams of particles are accelerated in the sequence of accelerating machines shown in Figure (2.2). The protons are obtained by hydrogen ionization. The first step in the LHC injection chain is the linear accelerator LINAC2 where the energy of 50 MeV 141 is Figure 2.2: Schematic view of accelerator system at CERN [38]. reached. Protons then go to the Proton Synchrotron Booster (PSB) and are accel- erated to 1.4 GeV . In the next step, 161 Proton Synchrotron (PS ) groups protons into the bunches separated by 25 ns and accelerate them to 25 GeV. Each beam is divided into 2808 bunches where each bunch consists of about 105 **1.15** ·1011 protons . After PS, the protons go through the Super Proton Synchrotron (SPS ) and reach the energy of 450 GeV . With that energy, 154 protons are injected into the LHC

before coming to the LHC. They are accelerated through the linear accelerator (LINAC3), Low Energy Ion Ring (LEIR) after which they go through PS, SPS, and LHC. Furthermore, the protons and ion beams 1 from the PS and SPS can be sent to fixed target experiments or to RD projects. The LHC ring consists of eight arcs and eight straight sections. The 115 region from the middle of the middle of the next 84 one arc to is called octant (Figure 2.3). At four out of eight straight sections, the beam crossings occur, and at these points, four experiments are placed: • CMS (Compact Muon Solenoid ) [39] and ATLAS (A Toroidal LHC AparatuS) [40] 69 general purpose detectors that can study large spectrum of physics; • LHCb (LHC beauty)[41] is an experiment designed for studying CP violation and asymmetry between matter and antimatter by performing analysis of rare decays of hadrons containing b 69 quark; • ALICE (A Large Ion Collider Experiment ) [42] is the **experiment** that studies heavy 69 collisions through the production of quark-gluon plasma. The other four points are 3 and 7 where the system for the beam collimation is placed, point 4

which consists of two radio-frequency systems for the particle acceleration, point 6 where the beam dump extraction

ring in two opposite directions. Besides protons, heavy ions can also accelerated through the chain of accelerators

deflecting fast-pulsed magnets and vertically-deflecting double steel septum magnets

125

Figure 2 .3: Schematic view of the LHC ring [36]. In the arcs of

45

the LHC, superconducting magnets are placed in order to bend the trajectory of accelerated particles. The magnets are made of niobium-titanium (NbTi) and cooled down to 1.9K using liquid hydrogen. The maximum magnetic field that can be reached is 8.3 T and this limits the achievable energy. In order to have the stable trajectory of the beam, multipole magnets are placed for stabilizing and focusing beams. 2.1.2 Performance of

LHC The number of collisions per unit of time at a collider is defined by the

11

relation: Niter = Lointer, (2.1) where ointer is the

cross section of the process and L is the luminosity of the machine. Luminosity is a very important parameter for the colliders and it can be written as: L

=  $4\pi \sigma \sigma V N1N2f Np$ , (2.2) if the transversal profiles ( $\sigma x$ ,  $\sigma y$ ) of the beams are the same.

N1 and N2 are the numbers of particles of each of two colliding bunches , f is the 44

frequency of evolution, and Np is the number of bunches. The integrated luminosity L for a specific time interval is defined as: t Lint = Ldt.  $(2.3) \int_0^1 dt$ 

In Figure 2 .4 the integrated luminosity collected by the CMS experiment in 2018 is shown

. Figure 2.4: Integrated luminosity collected by CMS in 2018 [43]. At the nominal conditions at LHC, the number of bunch crossing oer second is of approximately 40 MHz, with

an average number of 20 proton-proton interaction per bunch crossing. The

73

effect of the overlapping interactions that are not coming from the hard scattering with the main interaction is called pileup. Since the bunches of particles are separated 25 ns and the response of the detector is not instantaneous, it is also possible to have overlapping of interaction coming from different bunches. This effect

is known as out-of- time pileup. The average number of interactions in

29

2018 was <  $\mu$  >= 32 as shown in Figure 2.5. Figure 2.5: Pileup distribution observed by CMS in 2018 [43]. 2.1.3 LHC operations The LHC started with the proton-proton collisions in 2009, while the first

collisions at the center-of-mass energy of 7 TeV were recorded in 2010 . Following 107 the schedule of LHC operations (Figure 2.6) the first period of

data taking referred to as the Run 1 period, lasted until 2012 included. During this period the

energy was 7 TeV in 2010 and 2011, and 8 TeV in 2012 . For the

8

Run 2 data-taking period (2015-2018) the

center-of-mass energy was increased to 13 TeV and the collected luminosity

74

was 136 fb1. The last stage of the so called LHC Phase 1 will be Run 3, which will start in 2022 and last for 3 years. The total integrated luminosity that will be delivered during this period is planned to be about 300 fb-1. In between different data-taking periods, it was needed to prepare LHC and detectors for higher energy and luminosity (Long Shutdown 1 and Long Shutdown 2). Phase 1 will also be followed by a long shut-down that will allow the preparation

of the detector and the machine for the High Luminosity LHC phase (HL- LHC

189

). During this phase, which is planned to start in 2029, the integrated luminosity of 3500 fb-1 will be reached. The

center of mass energy will be increased from 13 TeV to 14 TeV

. New data-taking conditions also include the increase of pileup by factor five compared to the one from Run 2. For the HL-LHC, the radiation level will be increased which is why it will be a highly challenging environment for the reconstruction of the events. In order to maintain the performance from Phase 1 and to deal with the harsh environment of HL-LHC, the detectors need to be upgraded. Figure 2.6: The timeline of the LHC operations [44].
2.2 Compact Muon Solenoid The Compact Muon Solenoid [39] is a multipurpose detector 56 located in point 5 of the LHC ring, at Cessy in France
, at around 100 m underground. It is a 22 m long and 15 m wide cylindrical detector that consists of several subdetector systems each with a specific role in the detection of particles and measurement of their momentum at the interaction point. The central part of
CMS is a 12.5 m long superconducting magnet that provides a magnetic field of 3.8 T
. Within the magnet, the tracking system, electromagnetic, and hadronic calorimeters are placed. Outside the magnet, muon chambers embedded in the steel return yoke are placed.
A schematic view of the CMS detector is shown in Figure 2 .7. Figure 2 .7: 78  Schematic view of the CMS
detector [45] 2.2.1 Coordinate system In order to describe the interactions inside the detector, it is necessary to have coordinate system. For CMS, a cylindrical
coordinate system is used with the origin at the point of interaction. The
y-axis is vertical and points upwards, while the x-axis is horizontal and points toward 185 the
center of the LHC ring. The z-axis point in anticlockwise beam direction. The x-y plane is called the transverse plane and the

projection of a vector in the transverse plane is determined by the

azimuthal angle φ formed with respect to the x axis. The angle between the

67

z-axis and particles momentum vector is the polar angle  $\theta$  (Figure 2.8).

According to these definitions, the momentum of particle can be divided in two components the longitudinal momentum (pz) and the transverse

momentum (pT) 41 Figure 2.8: The longitudinal and transverse view of CMS detector. which is defined as: pT = p2x + p2y. (2.4) The energy transverse to the beam direction is denoted as ET and

the imbalance  $\sqrt{}$  of energy measured in the transverse plane is denoted by

35

ETmiss. For describing the angular distribution of particles the variable called rapidity (y) is used: y = In 1 E + pz 2 ( E - pz ) . (2.5) In case of ultra-relativistic particles (p  $\gg$  m) an approximation can be made and a variable named pseudorapidity (η) can be used:

 $\eta$  = - In tan θ 2 . (2.6) ( ) The angular distance between particles is defined as:  $\Delta R = \Delta \varphi 2$  174 +  $\Delta \eta 2$ . (2.6)

.7) √ 2.

2.2 Superconducting solenoid The superconducting magnet [46], which is the core of the CMS detector

, is operating at the temperature of 4.5 K and provides the

magnetic field of 3.8 T in the inner part of the experiment. The

12

magnet coil, with

(NbTi) conductor reinforced with an aluminum core. Outside the magnet the steel return yoke is placed. It consists of five barrel layers and three disks for each of the endcaps. The 99 yoke guides the magnetic field of 1. the region outside of the magnet . A map of the 8 T in 144 magnetic field is shown in Figure 2 .9. Figure 2 The magnetic field .9: 66 produced by a superconducting magnet. The right part presents the lines of the field, while on the left the strength of the magnetic field is shown [47]. The design of the whole CMS experiment is based on the solenoid. In order to have the least possible amount of material in front of the tracker system and calorimeters , these subdetectors 104 placed inside of solenoid . Due to the limited space, the calorimeters are designed to have a high density so that the electromag- netic and hadronic showers can be exhausted in the volume of calorimeters. 2.2.3 Tracker The part of the CMS experiment closest to the beam is the tracking system . It is composed of pixel detector and a strip 19 tracker, has a radius of about 1.2 m and a length of 5 147 [48, 49]. The role of the tracking system is to measure the trajectory of particles , with the precise determination 6 of their

momenta and vertex position. This part of the detec- tor needs

to distinguish the primary vertex that corresponds to the hard interaction from the

124

additional interactions coming from the pileup. The displaced vertices, coming from decays of heavy particles, such as  $\tau$  leptons and B hadrons, should be also identified. Because of the large luminosity and proximity to the interaction point, this part of the detector system is exposed to a large radiation. Therefore, the choice of the material for the tracking system is very important. In addition, the structure of this system needs to be optimized so that the

amount of material in front of the calorimeters is minimized. In order to fulfill the

79

requirements, both pixel and strip detectors are made of silicon and have different granularity for different positions in the detector system. The longitudinal scheme of the tracking system

is shown in Figure 2 .10. Figure 2 .10: Schematic view of CMS tracker

78

layout [50]. The pixel detector The pixel detectors with pixel dimensions of 100 × 150 µm2 are placed

closest to the interaction point (r  $\leq$  10 cm), and cover the pseudorapidity region of | 120  $\eta$ | < 2.5

. In order to be able to cope with the increased luminosity, the pixel detector has been upgraded

during the extended LHC technical stop in 2016/2017 [51]. The upgraded pixel 12 detector

has four layers in the barrel region instead of three,

at radii of 2. 9, 6.8, 10.9, and 16 cm , and three disks on each of the

from the center of the detector (Figure 2.11). The barrel region consists of

65

1185 segmented silicon sensor modules (BPIX), while in the forward disks there are 672 modules (FPIX). Each of the modules has a sensor with 160× 416 pixels connected to the readout chips (ROCs). Figure 2.11: Comparison of the upgraded pixel detector with the original one. The strip detector The pixel detectors are surrounded by a strip detectors system divided into 10 different regions. In the barrel region, with the

 $\eta$  < 2 .6 the Tracker Inner Barrel (TIB) and Tracker Outer Barrel (TOB

62

) are placed. The TIB covers the range

20 cm < r < 55 cm and is made of four layers of silicon sensors. The

66

thickness of sensors is 320  $\mu m$  and the inter-strip distance goes from 81 to 118  $\mu m$ . TOB, placed to cover a region 55 cm < r <120 cm, consists of 6

layers of silicon sensors with a thickness of  $\,$   $\,$  550  $\,$   $\,$   $\mu m$   $\,$  . Their  $\,$  inter-strip distance varies from

from 1

120 to 180 µm. The

sensors in the TIB and TOB regions have a rectangular shape. The size of the sensors differs according to their position, in the inner region, it is 6×12 cm2, while in the outer region size it is 10×9 cm2. The

endcap region of the strip detector consists of the Tracker Inner Disk (TID

6

) and the Tracker Endcaps (TEC). In the TID the sensors with the thickness of 320  $\mu$ m are used and are divided into 3 disks. TEC is made of nine disks where the thickness of the sensors depends on the distance from the center of the detector (from 320  $\mu$ m to 500  $\mu$ m). The sensors in the endcap regions are wedge shaped.

**2.2** .4 The electromagnetic calorimeter The ECAL [52] is a hermetic, homogeneous , 51 and high granularity calorimeter

dedi- cated to the measurement of the

energy of electrons and photons. It is made of lead tungstate (PbWO4) crystals 80 material is convenient because of its fast light emission and resilience to irradiation. Due to its short scintillation time, about 80% of light can be collected in 25 ns 90 . In addition, because of the properties such as high density (8.8 g/cm3), small Molier radius (2.2 cm), and short radiation length (0.89 cm ) of the 170 PbWO4, it was possible to construct a very compact calorimeter with high granularity. The total number of 75848 trapezoidal crystals is divided into a barrel area (61200) and two endcaps (7324 each). The longitudinal view of the **ECAL** is shown in Figure 2.12. The barrel region of the detector covers a rapidity 13 to  $|\eta| < 1$ .48. The length of the crystals in the barrel region is 23 cm which corresponds to 25.8 122 radiation lengths (X0), and the surface that they cover is  $22\times22$  mm2. The endcaps cover range  $1.48 < |\eta| < 3.0$ . The crystals in this region are 22 cm long (24.7 X0), with the front face area of 28.6 x 28.6 mm2. Figure 2.12: Schematic view of the longitudinal layout of ECAL detector . The crystals in the 195 barrel area are forming modules (400 or 500 crystals in one module), which are then grouped into supermodules. Supermodules 1 cover half of the barrel length and 20 in  $\phi$ 

. In the endcap regions

crystals are arranged into units of 5×5 crystals called supercrystals , which are forming two

semi-circular dees. The longitudinal view of ECAL is shown in Figure 2.13.

In front of each endcap, a preshower detector (ES) is placed . They are

covering the pseudorapidity range of 1 .65 < |  $\eta| < 2.6$ . The preshower detector consists of two layers of lead

plates with the radiation length of 2X0 and 1X0 and two layers of silicon strip detectors. The ES helps to distinguish the photons coming from the pion decayfrom single photons and to identify electrons from minimum ionizing particles. Figure 2.13: Schematic view of the ECAL structure. The scintillation light emitted by the crystals is amplified and collected by the fast, radiation-tolerant photodetectors. Because of the different magnetic fields and radiation flow in the different regions of the detector, two types of photodetectors

are used. In the barrel region the avalanche photodiodes ( APD) and in endcaps
vacuum phototriodes ( VPT) are

used. Since crystal response and the APD gain are temperature dependent, the temperature is stabilized at 18°C using the cooling system. 2.2.5 The hadronic calorimeter The part of the detector which measures the energy of charged and neutral hadrons is a hadronic calorimeter placed in between ECAL and the solenoid [53]. Besides measuring the energy of

hadrons by estimating the energy and position of produced hadronic jets , HCAL contributes to the missing energy determination

. To perform these measurements with good precision, HCAL needs to be hermetically closed, which means that it must cover the largest possible solid angle. The pseudorapidity range covered by the HCAL detector is up to  $|\eta|$  = 5.2. Since the ECAL

covers the range up to  $\eta=3$ , in the forward region of HCAL the electromagnetic 142 energy is

also

measured. The HCAL is composed of alternating layers of absorber and scintillator

118

materials and it is divided into four different regions (Figure 2.14). The Barrel Hadronic Calorimeter (HB) covers the

pseudorapidity range of  $|\eta| < 1.4$  while the endcap hadronic calorimeter ( HE ) cover the range

up to  $|\eta|$  = 3. In these regions, the absorber material used is brass (10% Cu and 30% Zn) which has short interaction length. The thickens of the absorber in HB is 5.8 and 10.6 interaction lengths for  $\eta$  = 0 and  $\eta$  = 1.3 respectively, while in the endcaps the thickness is 10.6 interaction lengths. The scintillation material is plastic.

Outside the solenoid the outer hadronic calorimeter which covers the range of | 191  $\eta$  | < 1

.4 is placed. HO is used to improve the confinement of hadronic showers. It increases the thickness of material so that hadronic showers are fully absorbed before the muon system. In order to have a high hermeticity of HCAL, the forward hadronic calorimeter (HF) is placed at the distance of 11 m

from the interaction point , to cover the range up to  $|\eta| = 5.2$ . HF is the Cherenkov based calorimeter with a steel absorber

and quartz fibers. Figure 2.14: Schematic view of the longitudinal layout of HCAL detector. The photodetectors used for the readout in HCAL are hybrid photodiodes in the barrel and endcaps region. The HO calorimeter uses silicon photomultipliers (SiPM), while in the forward region the Cherenkov

light is read out by photomultiplier tubes . The energy resolution of HCAL + ECAL is 51

the test beam with high energy pions and it is parametrized as :  $\delta E$  84.7%  $E = \sqrt{\oplus 7.4\%}$ . (2.8) E The first term in the formula represents the stochastic effects, while the constant term corresponds to the effects independent of the energy, such as imperfect calorime- ter calibration. 2.2.6 Muon system Since the muons are particles that can penetrate several meters of material without being absorbed, the subdetector systems of CMS described above can not stop them. The muons are detected in the tracker system, they loose a small amount of their energy in the calorimeters and are finally detected in the muon system placed at the

outermost part of the experiment [54]. The muon system, shown in Figure 2 .15, is

1

made of three different types of detectors:

Drift Tubes (DT ) chambers in the range |  $\eta$ | < 1.2, Cathode Strip Chambers (CSC ) for 0.9 <  $|\eta|$  < 2.4 and Resistive Plate Chambers (RPC

) that cover the pseudorapidity range

up to  $|\eta| = 1$  .6 Drift tube chambers are placed in the central part of the

detector and they are organized in four stations intertwined with the return yoke which provides a uniform magnetic field. The four stations are placed at the distance of 4.0, 4.

9, 5.9, and 7 m from the interaction point

29

and consist of 250 drift tubes in total. The basic constituents of DT are drift cells filled with a mix of argon (85%) and CO2 (15%). The dimensions of drift cells are 13 42 mm2. Each of the cells consists of an × aluminum "I" - shaped cathode and a stainless steel anode. After passing through a cell, a muon ionizes the mixture of gas, and by measuring the drift time of the electrons the position of muon can be determined. In the endcap region where the magnetic fields are less uniform and the flux of particles is large, the CSC detectors are used. The cathode chambers have a

Figure 2 .15: Schematic view of the longitudinal layout of the muon detector system . 32 trapezoidal shape, with

dimensions that vary with their position in the detector (the largest ones are 3.4 ×1.5 m2). In the four layers (ME1-ME4) 468 CSCs are deployed. The cathode

chambers consist of seven cathode panels and six anode wire planes. The

space in between layers is

filled with a mix of Ar (40%), CO2(50%), and CF4 (10%). The cathode

165

strips are placed in the radial direction which allows

measurements in the r-φ plane , while anodes wires are almost perpendicular to the strips

and that allows measurements in  $\eta$  plane. When passing through the CSC, muon creates an avalanche which induces a charge on cathode strips. The spatial resolution of this detector is ranging from 30  $\mu$ m to 150  $\mu$ m. The RPC detectors, which cover both barrel and endcaps regions, are composed of 4 bakelite layers that form 2 mm wide gas gaps. These gaps are

filled with the mixture of C2H2F4 (95.2%), C4H10 (4.5%) and SF6 (0.3

%) . The barrel part has 480 RPCs while in the each of the endcaps 288 chambers are distributed across four layers. The space resolution obtained in RPC detectors is not as good as in other detectors from the muon system, but the time resolution is excellent and better than 3 ns. 2.2.7 Trigger

At the center-of-mass energy of 13 TeV and with a luminosity of 1034cm-2s-1, the 129

LHC produces close to a 40 millions collisions each second. The collision rate is 40 MHz and for each collision, there are 20-50 simultaneous events. Because of the technical limits in data processing and storage, it is not possible to store information from all events. Since not all of the events are of interest for physics studies, a trigger system was developed to keeps interesting events and discards the others. The CMS trigger works in two stages: the

123

Level 1 (L1) trigger, which reduces event rate to 100kHz

and the

**High Level Trigger (HLT), which reduces** to event **rate to** 1 kHz. **The** L1 **trigger** operates at **the** hardware level **and** 

62

involves calorimetry and muon system. It performs a fast readout and selects events that have ionization sig- nals in the muon system or energy clusters in calorimeters. The information from calorimeters and muon detectors are processed in two separate flows as shown on the flowchart of the L1 trigger in Figure 2.16. Muon candidates are built in the muon trigger flow, while the calorimeter trigger builds photons, electrons, jets, tau candidates, and also the variables missing transverse momentum and the transverse sum of the jets above a specific threshold. The information is then combined and

passed to the global trigger , where the final decision is made. The final selection is based

on a specific menu made of 128 algorithms, which selects a specific type of

1

object and pass them to the HLT. The time used to make a decision about rejecting or selecting events is 4 µs. For the events that passed the L1 Trigger, the full readout of the CMS detector is performed and the HLT, which is implemented at software level, is used to further suppress the event rate. The HLT object reconstruction is based on the software used for the standard event reconstruction, but the configuration is optimized in order to have a faster reconstruction. To deal with the information coming from L1, HLT runs on a computer farm with 13000 CPUs. The HLT objects are using L1 objects as a seed. A given sequence of requirements performed by the HLT reconstruction algorithm is called a "HLT path" and it is used for selecting events of interest for a specific physics analysis. For both L1 and HLT, it can happen that the trigger rate is too high. In that Figure 2.16: A flowchart of the L1 trigger. case,

only a fraction of the events is accepted and the specific trigger is said to

152

be "prescaled". 2.3 Physics object reconstruction After the collisions, created particles go through the detector leaving a specific trace in the subdetector systems of CMS. The interactions of different types of particles in the subdetector systems are shown in Figure 2.17. A muon produces hits in the tracker and muon system, an electron produces

hits in the tracker and an electro- magnetic shower in the ECAL while charged hadrons

72

produce hits in the tracker and energy deposit in HCAL. Photons and neutral hadrons do not produce hits in the tracker but only electromagnetic shower and energy deposit

in the ECAL and HCAL respectively. The reconstruction of particles in the CMS 81 experiment is

based on the

Particle Flow (PF) algorithm [55 ]. This algorithm collects information from the subdetector systems and combines them to reconstruct

all the particles produced in the collisions. Figure 2.17: Slice of CMS detector experimental with the particles signature in the subdetectors. 2.3.

1 Track and vertex reconstruction The reconstruction of the trajectory of the charged particles in the

tracker system uses iterative methods to achieve high tracking efficiency. The first step in the reconstruction is the initial seed generation, where the initial track candidate and trajectory parameters are determined. The hits from all tracker layers are then gath- ered along the trajectory in the track finding (pattern recognition) step. Compatible hits are found using Kalman filter. A final fit is then performed which provides the best possible estimate of the track parameters: origin, transverse momentum, and direction. Quality flags are set based on specific criteria for the tracks

such as the number of hits or quality of the fit. Using the reconstructed track

the position of the interaction point (vertex) is determined. The requirement for vertex position is to have at least two reconstructed tracks within a distance of 2 mm from that position. Using the z coordinate of the tracks it can be distinguished if they are coming from hard scattering or from pileup interactions. Vertex associated with the hard interaction is called primary vertex while the vertex coming from pileup is the secondary vertex. The primary vertex is determined as one with the largest charged particles energy flow. 2.3.2 Calorimeter clustering The energy and the position of electrons, photons, charged an neutral hadrons is measured in calorimeters. These particles deposite their energy in the calorimeter cells. For particle reconstruction in the calorimeters, the clustering algorithm is used. This algorithm starts with determining a "seed", which is the calorimeter

cell with the energy larger than a specific threshold and larger than the energy deposited in surrounding cells . Then, the neighbouring cells	110
, with the energy above the fixed threshold, are included in the cluster. Finally, an expectation-maximization	algorithm
is used to reconstruct the clusters within a topological cluster	50
. 2.3.3 Muons The reconstruction of muons is done using	
information from the tracker and from the muon system . Depending on the subdetector system where they are	r 100
detected, muons can be: • stand-alone muons - reconstructed using the information from muon chambers muons - reconstructed in the tracker, where the	onlyl • tracker
track is compatible with at least one track segment in one of the muon detectors; • global muons - the track from the inner tracker is compatible with the one in	51
the muon chambers. 2.3.4 The particle flow algorithm description A particle created in a collision can leav few of the subdetector systems. It can be detected as	e traces in a
a track in tracker system , create calorimeter clusters, and (or) a track in muon system	15
. In order to avoid double counting of articles, the specific link algorithm is used to reconstruct them. By dedistance between	fining the
elements in the event, the quality of the link is estimated. If the link satisfies the	31
criteria, the flow of reconstruction starts and it is performed in several staps. The first stap is a collection of	f muono the

criteria, the flow of reconstruction starts and it is performed in several steps. The first step is a selection of muons, the compatible track and calorimetric deposit of muon is removed for the rest of the algorithm. After that, the reconstruction of electrons is performed. If an electron passes identification criteria, its

track and ECAL cluster are removed from the algorithm. The charged hadrons are determined by matching the

clusters created in ECAL and HCAL, which are compatible with the momentum measured in the tracker system. If there are no matched signals from the tracker, the neutral hadron or photon is created. Finally, the photons are reconstructed from the remaining clusters created in ECAL. 2.4 CMS upgrade for HL-LHC In order to maintain a good performance and to deal with the harsh environment of the HL-LHC described in Section 2.1.3, the CMS detector

needs to be upgraded. The Phase II upgrade for CMS includes: • the replacement of the

entire tracker with a new detector with higher granular- ity and better resistance to radiation. In the inner tracker, the new pixels will be smaller and the sensors will be thinner which will contribute to the better separation of tracks as well as to the improved impact parameter resolution. Since there will be additional pixel disks (up to 10), the pseudorapidity coverage of the tracker

will be extended to  $|\eta|$  = 4. The outer tracker will be

lighter, with shorter silicons sensor strips than current ones. Furthermore, with the new design of the module, the L1 trigger information will be available at the tracker level [51]; • the replacement of the calorimeter endcaps with a silicon-based High Granular- ity Calorimeter (HGC). The electromagnetic part will have tungsten absorbers, while in the hadronic part the absorber will be made of lead [56]; • new detectors in the muon system.

In the region, 1  $.5 \le |\eta| \le 2.4$  with the four chambers of

CSC, new four stations will be added equipped with Gas Electron Multiplier (GEM) chambers and Resistive Plate Chambers (RPC). This will

improve momentum resolution for the standalone muon trigger, the matching with the tracks for global

muons, and will provide better timing resolution. The acceptance of the muon system will be increased by additional GEM detectors in the space behind the new endcaps [57]. • the new electronics for the L1 trigger system. The latency of the L1 trigger will be increased from the current 3.4 µs

to 12.5  $\mu s$  , which will provide enough time for track reconstruction and matching tracks to  $\boxed{14}$  the information from the

calorimeters or the muon systems. In addition, the L1 trigger rate will increase from 100 kHz to 750 kHz [58]. Because of the higher rate, the electronics from the subdetectors will also need to be upgraded. The details about the ECAL readout electronics upgrade are in section 3.6. Chapter 3 ECAL Calibration The CMS electromagnetic calorimeter measures the energy of photons and electrons with an excellent resolution, that played important role in the

discovery of the Higgs boson through the  $H \rightarrow \gamma \gamma$  channel during the

136

1

LHC Run 1 period [59]. The great performance of ECAL is also crucial

for many analyses involving physics beyond SM such as high-mass resonances or detection of final states with energetic

electromagnetic particles [60], and for SM precision measurements [61]. The energy and signal reconstructions in ECAL are described in sections 3.1 and 3.2. Since the response of the ECAL varies with the time due to the crystal transparency variation induced by irradiation, constant calibration of the detector was performed during

Run 1 and Run 2 in order to keep the excellent performance of

this detector. The laser monitoring system used for monitoring the crystal transparency is described in Section 3.3. Part of my PhD work was devoted to the intercalibration of ECAL using the  $Z \rightarrow e+e-$  decays. The intercalibration constants were obtained for all three years of the Run 2 period. In addition, I was working on resolution studies for the Run 2 period and a comparison of the performance of ECAL during Run 1 and Run2. In section 3.4 the intercalibration methods are described while in section 3.5 the  $Z \rightarrow e+e-$  method is described in more detail. The plans for ECAL barrel readout electronics, for the HL-LHC are described in Section 3.6. 3.1 Energy reconstruction At the CMS experiment

electrons are reconstructed combining the measurement from the tracker and the ECAL [62], while the

reconstruction of photons, in absece of convertion in the tracker material is performed only with ECAL [63]. The electrons and photons produce a shower of secondary particles in the PbWO4 crystals. On average 94% of the total energy of the electron or photon entering the calorimeter is deposited in 3×3 crystal matrix centered on the hit crystal,

and 97% in 5×5 crystal matrix. Since electrons and photons can undergo respectively bremsstrahlung and photon conversion in the tracker material and because of the presence of a strong magnetic field, the electromagnetic shower is spread over more crystals.

## In order to take into account the spread of the energy

78

1

, the reconstruction is done using clustering algorithm. This algorithm starts with grouping together crys- tals with an energy greater than a specific threshold ( $\approx$  80 MeV for EB and 300  $\approx$  MeV for EE) in one cluster. The cluster which contains most of the energy deposited in a specific region is called the seed cluster. Because of the showering of electrons and photons when transversing the tracker, clusters are grouped into the superclus- ters (SC) belonging to the original electron or photon. SC is formed by grouping together clusters from the specific geometric area around the seed cluster. The Su- perclustering step combines two different algorithms to form SCs: the "mustache" algorithm which uses information from preshower detector and is used to measure low-energy deposits and the "refined" algorithm which uses information from the tracker and is used for determining the electron and photon objects quantities [64]. The reconstruction of the energy of photons and electrons is rather complete (around 95%) even for the electrons

or photons that undergo bremsstrahlung or conversion in the material in front of ECAL. 187

energy in a supercluster can be expressed as: Ee/ $\gamma$  = Fe/ $\gamma$  G · Ci · Si(t) · Ai + EES . (3.1) [ $\gamma$ i] 36

The sum runs over all the crystals that belong to the supercluster and the

terms represent: • Fe/y - supercluster energy correction that accounts for several effects such as

biases in the energy reconstruction due to the geometry of detector , leak- age of the 1

electromagnetic shower, and the clustering of energy emitted by bremsstrahlung or photon conversions. The small difference in

shower devel- opment of electrons and photons is also taken into account by this factor; • G - the conversion factor between ADC counts and energy, prior to any radia- tion damage. Two different values are derived for barrel and for endcaps from  $Z \rightarrow e+e$  decays ( $\approx 40 \text{ MeV/ADC}$  in EB and  $\approx 60 \text{ MeV/ADC}$  in EE); • Ci - the intercalibration term which

account the changes in response of crystals; • Ai - the reconstructed amplitude in ADC counts; • EES - energy deposited
in the preshower , zero in the region not covered by this detector. 3 .2 Signal reconstruction The
scintillation light emitted by PbWO4 is
measured by the photodetectors and read out as an analog signal by the front-end electronics. 1  The electrical signal
from the photo-detectors is pre-amplified, shaped, and processed by a multi-gain pre-amplifier
. The output is sampled at 40MHz and digitized by a 12-bit ADC. Ten consecutive samples are stored in the recorded events. For estimating the signal amplitude, during the LHC Run 2 period, a new algorithm called "multi-fit" was developed [65]. The method used during
Run 1 was not suitable because of the increased pileup 108
during Run 2. The
multi-fit algorithm estimates the in-time signal amplitude and up to 9 out of time amplitudes by the minimization of a $\chi 2$ , given by
: 10 M $\chi 2$ = j=1(Ajpij - Si)2 $\sigma$ S2i , (3.2) i=1 $\sum \sum 59$ where Aj are the amplitudes of up to ten interactions. For each bunch crossing j, the so-called pulse templates pij have the same shape of the in-time signal and differ by 25 ns shift in time. The
total electronic noise Si and its associated covariance matrix σSi are measured from dedicated pedestal runs. The least -square method is used to perform the χ2 minimization

. The

equalizes relative differences in the crystal response; • Si(t) - the time dependent transparency correction that takes into

fitted amplitudes are all constrained to be positive. Examples of one fit for signals in the barrel and in the endcaps are shown in Figure 3.1, for an average pileup of 20 and for 25 ns bunch spacing. The

33

red distributions represent the in-time pulses while the other light colors represent the out-oftime pulses with positive amplitude . Distribution in the dark blue color corresponds to the sum of all fitted contributions

.

Figure 3 .1: Example of fitted pulses for simulated events with 20 average pileup interactions and 25 ns bunch spacing, for a signal in the barrel (left) and endcap ( right

109

). 3.3 Laser monitoring The main source of ECAL response degradation is damage to the crystal and to photodetectors due to the high radiation level produced at LHC collisions. The optical transmission within the crystals is affected by the color centers produced by the ionizing electromagnetic radiation, which leads to the reduction of transparency of the crystal. The color centers partially anneal with thermal energy which is why the light output partly recovers during LHC

inter-fills and technical stops. The crystal transparency is monitored during data taking 126 with a laser monitoring system

, which provides a measurement of the crystal and photodetector response every 40 minutes [66]. A blue laser (447 nm) is used to measure and correct for changes in crystal and photodetector response. The laser light is directed to crystals using the system of optical fibers and splitters. At the last splitting stage, a bundle of 200 fibers called "harness" directs the light into 200 crystals and two PN diodes. The variation in transparency is measured through the ratio between the amplitude measured by the photo-detectors on the crystal and the

one measured with the PN diodes. The evolution of the relative crystal response to laser light

1

for Run 1 (2011-2012) and Run 2 (2015-2018) is shown in Figure 3.2. By construction, the first point is set to one. The response variation is shown for different pseudorapidity regions. The loss of transparency is larger at the very forward

region because of the higher absorbed dose of radiation in that part of the detector. The response change observed in ECAL channels

is up to 10% in the barrel region, 50% at  $\eta$  = 2.5 which is the limit of the tracker acceptance 95, while the changes go up to 98% in the region closest to the beam pipe. The recovery of the transparency during the periods without collision is also visible. The transparency is

measured continuously in parallel with the collision data taking. The time dependent corrections are derived on the fly from the measured response to the laser light. The correction for the i-th crystal at time t is given by:  $\alpha$  LCi(t) = Ri(0) [ Ri(t)]. (3.3) The response Ri(0) is the response to the laser light at the beginning of data taking each year and the parameter  $\alpha$  is taking into account the difference in the optical paths between laser and scintillation light. The laser corrections are used in the event reconstruction which occurs 48h after a run is ended. The stability of the energy scale is monitored using the diphoton invariant mass in  $\pi 0 \rightarrow \gamma \gamma$  decays and by

comparing the energy measured in ECAL to the track momentum measured in the tracker (E/p

1

) in W  $\rightarrow$  ev. The

stability plot obtained with the  $\pi 0$  method using the 2017 dataset is shown in Figure 3.3, 1 where the

ratio of diphoton mass and  $\pi 0$  mass is shown before and after applying the laser corrections. Figure 3.2:

Relative response to laser light (440 nm in 2011 and 447 nm from 2012 onwards) injected in the

ECAL crystals, measured by the ECAL laser monitoring system, averaged over all crystals in bins of pseudorapidity. The bottom plot shows the instantaneous LHC luminosity delivered during this time period

## . 3.4 ECAL intercalibration The

electromagnetic calorimeter is designed to provide good energy resolution for photons and electrons. The

106

resolution can be expressed by the formula:  $\sigma(E)$  S E =  $\sqrt{(3.4)}$ 

E 

N E 

C, where S is a stochastic term that includes statistical effects, N corresponds 1 the electronic noise contribution, while the C parameter is a constant term related to the calibration of the calorimeter . In order to measure the 1 of ECAL in ideal conditions performance , a test beam was performed before its installation in CMS [67]. During the test beam, there is no magnetic field and no material in front of ECAL and the 49 the electrons energies range from 20 to 250 GeV are used. The parameters obtained are: S = **2.8%, N = 12%, and C = 0.3** %. For high **energy** photons, the constant term is 133 expected to dominate the energy resolution. The design performance of ECAL corresponds to an energy resolution of 1% for photons from a H  $\rightarrow$   $\gamma\gamma$  decay which 62 Figure 3.3: The stability of the relative energy scale measured from the invariant mass distribution of  $\pi 0 \rightarrow \gamma \gamma$ 51 decays in EB and plotted as a function of time, over a period of 3 hours 121 during an LHC fill. is why the constant term must be kept below 0.5 %. The main contribution to the С 51

from the non-uniformity of the light collection , instabilities in the operation of ECAL, 179 and the

intercalibration constants accuracy. The intercalibration is performed continuously. Several independent methods have been developed to compute the IC constants,

and the resulting constants are combined to provide the final number for each crystal.

These methods are: • the \$\phi\$ symmetry

#### method -

based on the assumption that the total deposited transverse energy (ET) is the same

for all the crystals at the same

pseudora- pidity (η ring). Usi∑ng this method

the average energy is equalized in channels located at the same value of  $\eta$  109

and

intercalibration in  $\phi$  is performed by com- paring the E T deposited in one crystal with the total transverse energy collected by  $\Sigma$ the crystals in the  $\eta$ -ring

. Although, this method can profit from 63 a large amount of data, it provides lower precision compared to other methods because of the presence of  $\phi$  asymmetric material in front of ECAL. This is why the  $\phi$  symmetry method is typically used for validation or for checking relative time drift. •  $\pi 0$  method - it uses  $\pi 0 \to \gamma \gamma$  decays to calibrate ECAL response. The  $\pi 0$ 

invariant mass distribution is fitted with a Gaussian function for the signal and with a fourth order polynomial for the background. The intercalibration constants are updated iteratively in order to correct the fitted mass value in each channel

. Since this method is based on low energy photons, the precision is limited by the electronic noise and by pileup events, with non-negligible background contributions. Because of these limitations the  $\pi 0$  method cannot be used in the region  $|\eta| > 2.5$ . • E/p method - compares the

highest precision in the barrel, but because of the statistical uncertainties, the precision is worse in the endcaps. • Z  $\rightarrow$  ee method - it uses the electrons from Z  $\rightarrow$  e+e- decays . In the endcaps, this method is the most precise one and is also used in the region not covered by tracker  $|\eta| \in [2.5, 3]$ . The Z  $\rightarrow$  e+e- dataset is small compared to other processes, which is why the statistical uncertainty is higher than in the E/p method. This method will be described in detail in the next section. 3.5 The Z  $\rightarrow$  e+e- calibration method The properties of the Z boson were measured by the LEP experiments with very good precision [68]. The measurements of its mass had relative uncertainty of 2·10-5:

MZ = 91.1876  $\pm$  0.0021 GeV (3.5)  $\Gamma$ Z = 2.4952  $\pm$  0.0023 GeV . Because of the precise knowledge of its properties, the

Z boson is a good candidate for measuring the performance of the detector. The  $Z \rightarrow e+e-$  method for calibration 64 of ECAL was developed for the Run 2 data-taking period by thr CEA-Saclay group. 3.5.1 IJazZ tool IJazZ is a tool that uses the Z resonance for measuring the energy scale and res- olution of the ECAL by probing the phase-space with a very fine granularity.

In order to use the available data in the best possible way, this

tool is based on the maximization of an unbinned likelihood [69]. The likelihood compares the lineshape of the recontructed invariant mass with the expected one. The resolution and the energy scale, which are vectors of free parameters in different regions of the detector, are determined in the fit. To obtain the likelihood of the invariant mass, a simula- tion with a realistic description of the background contributions and detector effects is used. Because of the complexity to model the energy resolution and the large number of free parameters, a simplified description of the invariant mass lineshape is used with the assumption that: • the underlying invariant mass distribution from Z boson is well modeled by non-relativistic Breit-Wigner distribution:  $1 \Gamma Z 1 \rho Z (M) = \pi 2 M - MZ + \Gamma 2Z$ ; (3.6) 4 • the energy response function of ECAL is described by a Gaussian distribution and the non Gaussian tails are neglected; • the

background contamination in dilepton sample is negligible. The probability distribution of the invariant mass is computed from a Voigtain function [70] which is a Breit-Wigner convolved with a Gaussian distribution. Since there is a large number of free parameters which can cause computational issues, an approximate form of the Voigtian function is used [71]. The invariant dilepton mass is calculated from the kinematics of the two leptons: mee =  $2E1E2(1 - \cos \theta)$ ,  $(3.7) \sqrt{65}$  where Ei is the energy of the two leptons while  $\theta$  is their angular separation. The energy scale ( $\mu$ i) and resolution ( $\sigma$ i) of i-th electron, which are two parameters of the Gaussian smearing. are defined as:  $\mu = \mu 1 \cdot \mu 2 \sqrt{(3.8)} \sigma = 0.5 \sigma 21 + \sigma 22$ .  $(3.9) \sqrt{10}$  obtain the a better fit and avoid the effect of asymmetric response tails due to the

energy loss in the material in front of ECAL or empty spaces between the

2

An example of the fit is shown in Figure 3.4. For the calibration of ECAL the

186

 $Z \to e+e-$  method is used for three different purposes: • absolute calibration and energy equalisation along  $\eta$  ( $\eta$  scale ); • intercalibration measurements along  $\phi$ ; • resolution estimation and IC combination. Figure 3.4: The fit performed in the wide (left) and adapted (right) invariant mass window. 3.

5.2 η scale calibration In the η scale calibration procedure, the energy response is equalized for each ECAL η ring. In the

barrel region of ECAL, there are  $170~\eta$  rings, while in the endcap region there are 39~rings. For defining the  $\eta$  scale the electrons that are less affected by bremsstrahlung and less dependent on the upstream material included in the simulation are used. The selection of these electrons

is based on the R9 variable which is defined as : E3 $\times$  3 R9 = ESC, ( 3 .12) where  $\boxed{156}$  E3 $\times$  3 is the

energy deposited

seed crystal in the supercluster. Since the tracker covers the endcaps only up to $ \eta  \le 2.5$ (  i $\eta$   $\le 117$ ), the $\eta$ -scale calibration 2	3
Since the tracker covers the endcaps only up to $ \eta  \le 2.5$ (  $i\eta  \le 117$ ), the $\eta$ -scale calibration 2	
is done with the reconstructed electrons in the tracker acceptance region and for	2
the very forward region the calibration is done with pairs of one electron and one supercluster,	
where the electron is in the tracker coverage. The fit	2
consists of three steps: the calibration of the pairs EB-EB, the calibration of EB-EE and EE-EE with EB parameters and SC with  η  > 2.5 with electron (SC pairs) with the ring energy scale	s fixed,
for  η  < 2.5 fixed. The fitting procedure is done for both data and simulation and	3
the η scale	
is defined as the ratio of the ring energy scale measured in data and in	3
simulation. The obtained η scale is used as a scale factor applied on the calibration constants for data. In Figure ratio of scale parameters in data and simulation is shown for the data sample from 2018. The energy scales are computed after all the corrections for time-dependent effects are applied. Results are shown for both low bremsstrahlung (Golden) and high bremsstrahlung (Brems) electrons. Figure 3.5: The	
ratio of scale parameters between data and simulation, in gray for	2

R9 >0.94 electrons and in green for R9 < 0.94 electrons. 3.5.3 Intercalibration along  $\phi$  The Z  $\rightarrow$  e+e- method is one of the methods used for equalizing the crystal energy response along  $\phi$ . Before derivation of intercalibration constant, the absolute  $\eta$ - scale is applied such that all  $\eta$  rings have the same average energy response. The fit is performed with a free energy scale parameter for each crystal and 20 resolution parameters as described previously. To reduce the number of free parameters within a single fit, the

fit is performed over bands of 10 η-rings overlapping one with another

2

. To ensure that the ICs are measured with each SC fully contained in the window, only the

scale parameters of the 5 rings in the center of the window are used as calibration constants

2

. This procedure is repeated in different  $\eta$  regions to scan the whole EB. The intercalibration map obtained with this method for 2018 is shown in Figure 3.6. Figure 3.6: Map of the intercalibration constants for ECAL barrel region. This method for delivering IC constants is sensitive to gaps between ECAL su-permodules (every 20 crystals around  $\phi$ ) where the energy loss is not fully recovered by regression [64]. Therefore it is needed to perform additional corrections to ac- count for this effect. This correction is derived by performing a fit on the whole EB, and

since the effect should be the same for all modules, folding

2

all the supermodules together and also the EB regions in positive and negative pseudorapidity are folded together. The results of this fit are shown in Figure 3.7. After using the results of the fit as a multiplicative factor to the ICs, the intercalibration map is corrected and shown in Figure 3.8. For calibration of endcaps, the

fit is performed over the full EE + and EE-, and no additional corrections are needed. The

2

calibration with this method is performed using 90 % of the available Z  $\rightarrow$  e+e events, the remaining 10% are used for validation. 3.5.4 Resolution and combination The final IC constants are obtained as a combination of constants derived from the methods described in Section 3.4. Each of these methods is using different datasets and has different statistical and systematical uncertainty. To obtain the Figure 3.7: Corrections applied to account for the effect of gaps between the super- modules. final intercalibration constants, a combination of the overall precision of each method with systematic uncertainties included is performed. The uncertainties for the  $\pi 0$  and E/p methods are obtained by estimation of the impact of the calibration on the lineshape of the Z invariant mass distribution for the Z  $\rightarrow$  e+e events. The Z  $\rightarrow$  e+e is chosen as the reference method because it is the least sensitive method for effects such as tracker momentum calibration, pileup, and upstream material. Therefore, the IC constants for specific method are computed as:

 $\sigma C = \sigma 2 ref + \rho - 2 \sigma E \ 2 - \sigma E \ 2$ ,  $(3.13) \ \sqrt{[(EC)(Eref)]}$  where  $\rho$  is a parameter that corresponds to the IC precision on the lepton energy resolution and  $\sigma E/E$  is the relative energy resolution per electron for method C. The combination of the constants obtained with different methods is done by attributing a specific weight for each method, where the weight is based on the relative IC precision: 1 wC =  $(\sigma C)2 \ k \ (\sigma k)2 \ 1$ . (3.14) Index k runs over different calibration m $\Sigma$ ethods: Z  $\rightarrow$  e+e, E/p,  $\pi 0$ . The precision of the combined ICs, assuming that all the methods are independent is obtained as:  $\sigma$  comb = 1 .  $(3.15) \ \sqrt{k} \ (\sigma k)2 \ 1 \ 70 \ \Sigma$  Figure 3.8: Final map of the final intercalibration constants for barrel and endcaps for 2018. The IC precisions obtained with different methods for all years from the Run 2 are shown in Figure 3.9. In the barrel region the  $\pi 0$  method is slightly worse than Z  $\rightarrow$  e+e and E/p method. In the endcaps, the most precise method is Z  $\rightarrow$  e+e. For the very forward region ( $|\eta| > 2.5$ ) which is outside of tracker acceptance, only the Z  $\rightarrow$  e+e method is used. For each year of the Run 2 data taking period of the LHC, a refined calibration of the ECAL was performed. The improvement after this calibration can be seen in Figure 3.10 where the electron energy resolution for 2018 is compared to the preliminary calibration performed at the end of each year and to the refined calibration. The resolution is shown as a function of pseudorapidity, where  $|\eta| = 0$ , 0.45, 0.8, and 1.15 corresponds to inter-module boundaries in the barrel. The evolution of resolution through the Run 2 is shown in Figure 3.11 where it can be seen that it is comparable during the three years. The esolution

for electrons from Z-boson decays is at the level of 1.7% in the central region of the ECAL and 3

92

% The o Figure 3.9: Overall precision of the different IC measurement methods as well as their combination

for 2016 (top left), 2017 (top right), and 2018 (bottom ). at large pseudorapidity. In addition, 12

resolution of Run 2 is compared with the one obtained in 2012 during Run 1. In Figure 3.11 the resolution is shown for the low bremsstrahlung electrons and the

samples are reweighted to match the pileup distribution from 2017

4

. It can be seen that despite the much larger instantaneous luminosity and ageing of the detector, the performance during

Run 2 is very close to the one from Run 1

4

. 3.5.5 Simulation studies The energy resolution has contributions from many different effects such as pileup, noise, accuracy of the calibration. In order to study these effects, dedicated simulated samples of  $Z \rightarrow e+e$  with specific

effect are produced: • simulated sample with calibration; • simulated sample with calibration and energy threshold; Figure 3.10:

Energy resolution as a function of the pseudorapidity for the 2018 dataset with the preliminary and refined calibration. Figure 3.11:

Energy resolution with the refined calibration as a function of the pseudorapidity comparing 4

2016, 2017, and 2018 data-taking periods (left) and Run 2 with 2012 data-taking 4

(right). • simulated sample with calibration, energy threshold and realistic noise; • simulated sample with calibratuon, energy threshold, realistic noise, and pileup. These studies are done assuming 2018 data-taking conditions. Using these samples it is possible to estimate the individual contribution of the different effects to the resolution, as shown in Figure 3.12. In addition, the cumulative ECAL energy resolution, which is obtained by adding up the different contributions to the resolution is shown. On these plots, the simulation is assumed to be ideal ECAL

simulation without electronic noise, without PU, and assuming a perfect ECAL calibration 92

. It can be seen that in the barrel region there is an almost equal contribution to the calorimeter resolution coming from

pileup, noise, and effects not included in the simulation (i.e. extra smearing ). In the endcap 92 region, the extra smearing effect is as large as the intrinsic energy resolution in the

ideal case. The inter-calibration precision has a negligible impact on the resolution. Figure 3.12: Contribution to the ECAL energy resolution from different effects on the (left) and cumulative energy resolution obtained by adding up the contribution from different effects. 3.6 ECAL upgrade for High Luminosity LHC In order to maintain performance from Phase 1 and to deal with the harsh envi- ronment of HL-LHC, the electromagnetic calorimeter of CMS needs to be upgraded [73]. The plan for the Phase 2 ECAL upgrade is a full replacement of the endcaps and upgrade of the barrel readout electronics. The current readout system of ECAL is shown in Figure 3.13. On each crystal in supermodule, there are two APDs that are connected to a Very Front End (VFE) card through a Kapton cable. VFE card consists of five readout channels with analog-to-digital converters (ADC) and multi-gain pre-amplifiers (MPGA). Three outputs with gains x1, x6, and x12 are provided for each channel by the MPGA, and conversion of outputs is done using the 12-bit, 40

The ECAL readout s	system. and the trigger generator circuit based on an ASIC. The
output is f	Further sent to the DAQ and trigger system using the optical transceiver FENIX 4
In order to deal wit	th the trigger latency of
12.5 µs (inst	tead of the current 4 .5 µs ) and trigger rate of 750 kHz
instead of the curr performance. The	rent 100kHz), the ECAL barrel electronics needs to be modified and designed to maintain good
schematic vi	iew of the updated electronic for ECAL is shown in Figure 3 .14. In the
upgraded electronic	es, the MPGAs from the VFE card
•	ced with the Trans Impedance Amplifier (TIA ) called CATIA [74]. This will 4 separation of the electromagnetic signals and the signals coming from the APDs . Instead of the multi-channel
APDs, new readout	electronics will have
LiTE-DTU AS at 160MS/s	SIC (Lisbon-Torino ECAL Data Transmission Unit ) [75]. This ASIC samples the signal with 12-bit resolution. The
upgrade will also in	clude moving the trigger primitive generation from the
	to the off-detector system. The upgraded FE card will use Low Power Gigabit  OGBT) optical transceiver [76] and Versatile Link plus

MS/s ADC chip. After the VFE, the signal is sent to the Front-End card that contains an optical transceiver Figure 3.13:

[77] for data transmission. The off-detector system will be

based on the Barrel Calorimeter Processor (BCP) card [78] and it will use FPGAs for 4 read-out of the detector and to generate trigger primitive. The prototypes for upgraded **ECAL** readout have been produced and tested while further tests are underway. The results of the tests of the CATIA prototype, performed in test beam campaigns at the H4/H2 beamline of the CERN SPS 4 [74], are shown in Figure 3.15. The measured resolution in the test beam matches with Figure 3.14: Schematic view of the new ECAL barrel electronics. the one obtained in the beam test for legacy electronics [79]. The timing resolution is measured to be better than 30 ps for the electrons with an energy above 50 GeV , which complies with 4 the specification. Figure 3.15: Energy resolution (left) and time resolution (right) obtained in the test beam campaign with the 4 CATIA ASIC connected to a commercial ADC [74]. Chapter 4 Measurements of track based event shape observables The Z boson production in association with jets is essential for the modeling and understanding 3 of QCD interactions. The comparison of the measurements with the MC simulations improves the understanding of the prediction limits. It is also useful for guiding the improvement of calculations and MC generator techniques. The

many Standard Model processes and for the processes beyond the SM. Therefore, the measurements of this process with the highest possible precision are very important. Several measurements and searches at LHC require vetoing background events based on their hadronic activity. In particular, in the case of a signal produced by vector boson

production of a Z boson in association with jets is also a

major background to

207

fusion, the low hadronic activity in the central region is typically exploited. The veto implies corrections from higher order QCD contributions, whose uncertainties are estimated by scale variations. Hadronic activity vetoes are typically based on jets,

yielding complicated phase space restrictions, and reliance on leading-log (LL) parton-shower 162

Monte Carlo

simu- lations. In order to get better controlled cross sections, a new method based on using event shape variables such as N-jettiness has been proposed [3]. The factorization formula allows the summation of logarithms to NNLL order to be performed. In this chapter, the

measurement of the differential cross section as a function of event shape variables and 138 the sum of the transverse momentum

of charged particles in events with Z boson production in dimuon decay channel is presented. These variables are computed with charged particles only in order to constrain the contri- butions coming from the pileup particles. The measurements are performed in four different transverse momenta (pT(Z)) regions and in three different dilepton mass (MII) regions. In the first part of this chapter (Section

**4.1), the** measured variables are described in more detail. In Section 4. **2** 

data samples and Monte Carlo simulated samples are presented. The selection criteria for the events and for the particles used for N-jettiness calculation are described in Section 4.3, while corrections applied to simulations are summarized in Section 4.4. The techniques for deconvolution of detector effects are presented in Section 4.5. The uncertainty sources that affect the measurement

are described in section 4.6. Finally , in Section 4.7

the results for differential cross section measured are presented. 4.1 Observable definition The inclusive event shape variable N-jettiness defined in [3] is a variable that gives a global view of the event. It is a variable that tests the compatibility of events with a topology with N jets and it can be used to discriminate signal from background with more jets. N-jettiness ( $\tau$ N) can be expressed as:  $\tau$ N = 2 Q2  $\tau$ 

k min qa · pk, qb · pk, q1 · pk, ..., qN · pk . (4. 1

) {} The sum runs over all final state particles except the signal leptons or photons and pk is the four-momentum of particle k. In here, qa and qb are four-momenta of the beams while q1,...,qN represents four-momenta of N jets in the event. The scale Q2 is the typical scale of the hard scattering process. The four product qab  $\cdot$  pk or qj  $\cdot$  pk represent the distance between final state particle with the momentum pk from the beam or jet j. The distance measure can be adapted for the particular case, while the general properties of the variable remain the same. The choice of the distance measure defines the shape of the area that is assigned to the jet. The closest distance between pk and beam or jet axis is the minimum of the Eq. 4.1. This estimated sum of minima has a small contribution from soft particles and from energetic particles that are close to jets or beams, while energetic particles that are far from jet and beam axes give a large contribution. For events with at least N jets, in the limit  $\tau N \to 0$  the event contains N narrow jets. In the case where the N-jettiness is further from 0, the jets are wider and there is radiation between beams and jets or the number of jets is higher than N. In this analysis, the zero-jettiness (also called "beam-thrust") and one-jettiness variables are computed using a geometrical measure in the reference frame where the Z boson rapidity is zero:  $\tau 0 = pTke-|yk-Y|$  (4.2)  $\Sigma k \tau 1 = \min pT k eY - \eta k$ ,  $pT k e- Y + \eta k$ , pT k (2 cosh  $\Delta \eta J 1, k - 2 \cos \Delta \varphi J 1, k$ ), (4.3)  $\Sigma k$  where Y is the rapidity of the boson, and  $\Delta \eta J 1, k$  and  $\Delta \varphi J 1, k$  are the pseudorapid- ity and azimuthal angles between particle k and jet. In addition to these variables, the

sum of the transverse momentum pk of final state particles with the signal components 212 excluded is

measured.  $\sum$  Since the N-jettines variable assigns particles to one of the jets or beams axes, it can be used as an exclusive jet algorithm. Therefore, in this analysis, the axes of jets are computed by minimizing N-jettiness. Minimization is performed using the XCone algorithm [80]. This algorithm starts with the seed axes that are obtained with the anti-kt clustering algorithm or by looping over all possible axes combinations to find the minimum (if anti-kt jets are not defined). These axes are iteratively improved by looking for a minimum of N-jettiness. Through this step, the particles are assigned to one of the jets or beams regions. Using the information from jet constituents, jet axes are recomputed and updated. The assigning and updating axes steps are repeated until the axes converge to some accuracy, which in this case is decided to be 10–4. 79

4.2 Data samples The analysis is based on data collected by the

148

CMS experiment from 28th of April to 3rd of December 2018

in proton-proton collisions at the energy of 13 TeV . This data set corresponds to an integrated luminosity of 59.4 fb-1

. Collected data are divided into different primary datasets according to the trigger selection and in this analysis, the DoubleMuon dataset is used. During 2018

with different beam and detector con- ditions (Table 4.1). The samples with the latest reprocessing of data and simulation with the most updated conditions (such as calibrations, energy scale corrections, etc) for all the subsystems and object reconstruction algorithms are used. Data sample L[fb-1] DoubleMuon Run A 13.704 DoubleMuon Run B 7.061 DoubleMuon Run C 6.895 DoubleMuon Run D 31.742

Table 4.1: List of data samples used in the analysis. The Monte Carlo samples for the

172

simulation of the signal and background pro- cesses are shown in Table 4.2. The signal samples are generated with the Mad- Graph5\_amc@nlo interfaced with pythia8, as explained in Section 1.4. In order to gain more statistics for the signal sample, the samples binned in the number of outgoing partons (npNLO) at matrix element level are merged with the sample with an invariant mass of leptons greater than 50 GeV. The

showering and hadronization are performed with Pythia8 using the CP5 Tune. The

132

matrix element (ME) is computed to NLO for up to two partons. The PDF set used is NNPDF 3.1 and the strong coupling as is set to 0.118. The cross section for these samples is obtained from the generator. The dominant background is the production of the top quark pairs that decay into leptons. This process, as well as the

single top production in the t channel and single top production in association with a W boson

13

, are simulated at NLO in αs 80 using the powhegbox [81]. The single top quark production in the s channel is simulated using MadGraph5\_amc@nlo with the αS at NLO, while the production of the Z boson in association with electroweak boson (Z or W) is simulated at LO with pythia8. As for the signal samples, showering and hadronization for background simulations are performed with Pythia8 CP5 Tune. In order to compare the signal and background simulations

with the experimental data, the simulated events are normalized according to the

37

observed luminosity of

the data samples. The weight factor used for normalization is computed as: weight =  $\sigma$ L (4.4) Nprocessed

.2,

L is the integrated luminosity of the data sample and Nprocessed is the number of generated events. The

72

cross sections are calculated at NNLO + NNLL using Top++ version 2.0 [82] for tt process and NLO in as using Hathor version 2.1 for single top production. The cross section for ZZ and ZW processes is calculated using MCFM 6.6 while the tW cross section is taken from the [83]. 4.3 Selection In this analysis, events with two opposite charged muons are studied. In order to reject the events coming from the background processes listed in Table 4.2, a specific set of selection criteria is applied. In addition, for the computation of N-jettiness variables, selections on particles are applied to exclude those coming from the pileup. 4.3.1 Event selection The events studied in this analysis are selected using the unprescaled trigger with the requirements for the transverse momentum of the muon candidate with the highest

pΤ pT to be greater **than** 17 **GeV and** for **the** second muon, the to be has greater than 8 GeV

47

. There is a loose tracker isolation requirement and the

invariant mass of leptons is required to be above the threshold 194

3.8 GeV. In addition, the Process  $\sigma$  [pb] Signal Z+jets (mll > 50 GeV) Z+jets (npNLO = 0) Z+jets (npNLO = 1) Z+jets (npNLO = 2) 5931.9 4620.52 859.59 338.26 Background tt tW tW WJetsToLNu t  $\rightarrow$  IX (s channel) t  $\rightarrow$  IX (t channel) t  $\rightarrow$ IX (t channel) WW  $\rightarrow$  2L2Nu WZ ZZ 831.7 35.6 35.6 61526.7 10.32 136.02 80.5 12.21 23.5 15.4

Table 4 .2: List of simulation samples used in the analysis

51

and their cross section. longitudinal distance between the two muon tracks (DZ) has to be lower than 0.2 cm. This trigger line in CMS is called: HLT\_Mu17\_TrkIsoVVL\_Mu8\_TrkIsoVVL\_DZ\_Mass3p8. The measurements are performed for the muon pairs

where the leading muon has pT > 25 GeV and the subleading has pT > 20 GeV. 167 The

criteria for transverse momentum is above the threshold of the trigger in order to reduce the

bias from the trigger efficiency . Both muons are selected within absolute pseudorapidity | 62 η

### | < 2.4. The muons

are identified using the PF algorithm described in Section 2.3. The selection criteria for 114 identification used in

this analysis correspond to the so called MediumID muons [84].

A medium muon is a muon that is either tracker or global 82 muon 72

that uses 80% of inner tracker layers it transverses. For the medium muons, the compatibility of the muon segment has to be greater than 0.451 for tracker muons and 0.303 for global muons. In addition, if the muon is global, the global fit needs to have  $\chi 2$  per degree of freedom

less than 3, the χ2 for position match between the tracker and standalone muon

less than 12. The medium muon also includes selection based on the kink-finding algorithm. This algorithm splits the track at several places and for each split compares two tracks. If the  $\chi 2$  is large, that means tracks are not compatible with the single track. The maximum value of the  $\chi 2$  is required to be lower than 20. The overall efficiency for the muons from W and Z events is 99.5%. The details of this identification requirement are summarized in Table 4.3. Variable Selection

Global Muon Yes Particle-Flow muon Yes  $\chi 2/$  ndof of the global-muon track fit

< 3 Tracker-Standalone position match < 12 Kink finder < 20 Segment comptibility > 0.45 Table 4.3: Medium ID criteria used for muon selection. In

order to distinguish the muons originating from the Z boson from the

25

117

107

ones produced in jets, the isolation criteria is applied. The relative muon isolation is determined as: Irµel = p1µT pTP V + max 0, h± ETh0 + ETy - 1 2 pTP U h±,  $(4.5) [\sum (\sum \sum)] \Delta$ 

R<0.4 where the sum runs over the PF candidates in a cone of radius  $\Delta$  R = 0.4 129 around the direction of the muon candidate track. The

energy contributions considered are the ones originating from primary vertex ( $h\pm PV$ ), neutral hadrons (h0), and photons (y). Since the neutral

particles deposit on average half as much energy as charged particles, the contribution of the neutral hadrons from

pileup is estimated as 1/2 of charged particles coming from pileup h±PU . For this analysis, the relative muon isolation is required to be lower than 0.15. 4.3.2 Track selection The N-jettiness variables as defined in Section 4.1 are computed using all final state particles besides final state leptons. In Figure 4.1 the 0-jettiness distribution is shown at the generator level and at the reconstructed level. At the reconstructed level, there are many particles coming from pileup that are contributing to the sum and shifting the peak of distribution toward the higher values. Figure 4.1: The distribution of zero-jettiness at the generator level (blue) and re- constructed level (red). Many particles measured in the final state originate from pileup and specific selections need to be applied to constrain them. Since the neutral particles are detected only in the calorimeter it is hard to distinguish particles coming from the primary vertex from the ones coming from the pileup. Therefore, in this analysis, only the charged particles are considered in calculations. To see the effect of choosing only charged particle, comparison of distributions of  $\tau$ 0 variable are computed with only charged particle, neutral particles and of  $\tau$ 0 computed with all the particles is performed at generator level (Figure 4.2). The number of particles in all three distributions is same and particles are selected randomly from event. The charged particles

are required to have pT greater than 1 GeV and |η|<2

.4. To suppress in addition charged particles from pileup, the further selections of particles are made according to their association with the primary vertex. The Figure 4.2: The distribution of zero-jettiness computed with charged, neutral, and all particles from the event different flags that show how tight the association with the PV are summarized in Table 4.4. PV association meaning PVUsedInFit PVTight PVLoose NoPV is the track that is used in the PV fit is the track that is not used in the fit of any of the other PVs, and is closest in z to the PV is the track that is closest in z to a PV other then the PV is the track that is used in the fit of another PV Table 4.4: PV association flags description.

In order to estimate the contribution of the tracks coming from pileup and the

205

196

ones that are coming from the main PV, for different PV association selection, dedicated studies are performed. Using the simulated sample, the tracks at the reconstructed level are identified as tracks from PV by searching for the generated particles that can be associated with them. If there is a generated level particle that can be matched with the one at the reconstructed level we consider that particle as the one coming from the main PV. For these studies, particles at the generated level and reconstructed level are considered to be matched if  $\Delta R$  between generator level particle and reconstructed particle is lower than 0.005 and the relative difference for reconstructed level and generator level pT is lower than 0.03. To be identified as a particle that comes from pileup, the reconstructed level particle is required not to be matched with any of the particles at the generated level, which in this case means to have a  $\Delta R$  distance greater

than 0.3 or to have a relative pT difference greater than 0

44

.2 with respect to the generator level particle. In Figure 4.3 it can be seen that most of the particles that originate from the main PV are used in the primary vertex fit or are closest in z to the main primary vertex. For the N-jettiness computation, only the particles that satisfy one of these two PV association qualities are considered. In addition, the selection based on the longitudinal distance of

track from the primary vertex is required to be lower than 0.3 cm

43

. Figure 4.3: Vertex quality association flag for matched and non matched tracks. With these selections applied, the particles coming from pileup are rejected while the efficiency of reconstructing particles is kept. 4.4 Monte Carlo corrections In

order to improve the agreement of simulation with data, several corrections need to be

100

62

applied to

Monte Carlo events. These corrections are applied as an event weight and include several effects such as pileup, misalignment of the reconstruction efficiency, correction factors due to the efficiency of muon identification and isolation selection, and trigger efficiency. 4.4.1 Pileup The average number of pileup events depends on the exact beam conditions and varies with the time during the acquisition run because the beam luminosity de- creases with time until LHC is filled again.

The pileup profile in data is estimated by using the instantaneous luminosity and the total proton-proton cross section

of 69.2 mb [85]. The pileup profile in simulated samples may not be exactly the same as the one in data since it is difficult to know it in advance to include it in simulation. Therefore, simulations

need to be corrected in order to match the pileup distribu-tion with the one from data 35.

The correction is

performed by delivering weights

as a function of the number of vertices per event

197

, which are then applied to simulation. 4.4.2 Rochester The measurements of muons momentum at the CMS detector are biased due to the

detector misalignment, software reconstruction , or uncertainties in the magnetic field. The so-called Rochester method

[86] is used to correct this bias. This method consists of two steps. In the first step, the mean inverse transverse muon momentum < 1/pT, $\mu$  > of muons

from the Z boson decays is required to be the same as the one derived from the

perfectly aligned sample. The corrections are derived as a function of charge, pseudorapidity, and azimuthal angle and they are derived for both data and simulation. As a second step, the average invariant mass < Mµµ > is used to tune the corrections and remove the bias coming from mismodeling of the detector efficiency in simulation. 4.4.3 Scale factors for ID and isolation Differences between data and simulation can be introduced by the selection criteria and imperfect modeling of objects used for these selections. The efficiency of isola- tion and identification selection described in Section 4.3 are computed for data and simulation

using the Tag and Probe method [87] as a function of the muon

117

trans- verse momentum and pseudorapidity. The correction factors, called scale factors (SF), which are applied as weight, are computed as:  $\epsilon$ data(pT, $\eta$ ) SF =  $\epsilon$ MC(pT, $\eta$ ). (4.6) 4.4.4 Trigger Scale factors To account for the efficiency of the trigger used in the analysis, the correspond- ing scale factors need to be delivered and applied to simulation. For the double muon trigger

used in this analysis , I calculated the scale factors using the "refer- ence trigger" method 119

that is suitable for complex trigger efficiency computation. In this method, the efficiency of the complex trigger is computed by estimating its efficiency for the events selected by reference trigger first. After computing the ref- erence

trigger efficiency, the double muon trigger efficiency can be then calculated for all events. The

first step in this method is choosing the reference trigger which should be the one that has high efficiency on the events that pass complex trigger. For the trigger used in this analysis, a good choice for reference trigger is

a single muon trigger with a pT threshold of 17 GeV. For the dimuon events 53

, the reference trigger efficiency is computed as:  $\epsilon ref = 1 - (1 - \epsilon ref \mu 1) \cdot (1 - \epsilon ref \mu 2)$ . (4.7) The efficiency of the complex trigger is computed for events that are selected with the reference trigger ( $\epsilon DMu|ref$ ). Finally, the efficiency of the double muon trigger efficiency is computed regardless of the reference trigger:  $\epsilon DMu = \epsilon DMu|ref \cdot \epsilon ref$ . (4.8) In simulation samples, the information of produced (generated) and reconstructed number of events is available, and efficiency is computed using this information.

In data samples, the efficiencies in data are calculated using the Tag and Probe

method

. The efficiencies are computed for the events that are passing selection de- fined in Section 4.3. In order to avoid the case where both muons are matched to the same trigger object, it is required that  $\Delta R$  between the two muons is greater 88 than 0.3. The efficiency measurements are performed as a function of the absolute pseudorapidity of muons. In the Tag and Probe method, the signal and background are modeled using the analytical function, which in this case are Gaussian for signal and exponential function for background. The fit is performed to model the invariant mass of muons. The example of fit for probe muons that are passing selection and for the ones that are failing selection is shown in Figure 4.4. Figure 4.4: Fit results for one of the central pseudorapidity bins for probe muons that are passing (left) and failing(right) selections. The computed efficiencies both in data and in simulation are shown in Figure 4.5. The uncertainties shown in these plots are including both statistical and systematical uncertainty. The systematical uncertainties include the uncertainties related to the modification of the histograms that are fitted, such as variation in the binning and range of the invariant mass histograms fitted, and uncertainties related to the fitting procedure, more precisely the fitting function used for signal fit. These uncertainties are added in quadrature. Figure 4.5: Single and double muon trigger efficiencies in data (left) and simulation (right) shown in bins of pseudorapidity. The final scale

factors, computed for this analysis and shown in Figure 4.6 are computed as: SFtrigger = εDMuData εDMuMC . (4.9) Figure 4.6: The scale factors obtained for UL2018 shown in bins of pseudorapidity. 4.4.5 Data - simulation comparison In order to estimate the contribution of the background, in this section, we com- pare the distributions of variables at the reconstructed level in data and simulations (samples from Table 4.1 and Table 4.2). Comparison of the data and Monte Carlo distributions also allows us to check the effectiveness of corrections applied to sim- ulated samples. Z boson variables Z boson candidate is reconstructed using two oppositely charged muons with the highest transverse momentum. The distributions are shown for events that pass selections defined in Section 4.3. For the invariant mass distribution shown in Figure 4.7, the invariant mass bounds are removed. It can be seen that after applying the Rochester correction, a good description of the invariant mass is obtained. In order to see the contributions of each background considered, the distribution of invariant mass is also shown in the logarithmic scale. It can be seen that in whole range, the background contributions are rather small. Figure 4.7: Data to simulation comparison of the

invariant mass distribution with linear(left) and logarithmic (right) scale. The distribution of the

Z boson rapidity and transverse momentum are shown in Figure 4.8. These distributions are shown for events with real Z boson with the invariant mass in the range from 76 to 106 GeV. The rapidity distribution shows good agreement between data and simulation, while in the low of pT (Z) (less than 30 GeV) the differences are observed. Figure 4.8: Data to simulation comparison of muon pair distributions: rapidity and transverse momentum. Muon variables The data and simulation comparison of the muon transverse momenta, pseudora- pidity, and azimuthal angle are shown in Figure 4.9. The distributions are shown for the muons from the events, therefore histograms are filled two times for each event. After applying all necessary correction factors, the distributions show good agreement between data and simulation. Figure 4.9: Data to simulation comparison of reconstructed muon distributions: transverse momentum, psudorapidity and azimuthal angle. Track variables The transverse momentum and pseudorapidity distributions of charged particles that contribute to the calculation of N-jettiness are shown in Figure 4.10. In the high pseudorapidity region, it can be seen that there is a discrepancy in data and simulation. Since this observable is sensitive to the non-perturbation effects ,addi- tional studies are done using the simulations with a different Pythia8 tunes. The transverse momentum and pseudorapidity distributions are compared at generator level for two different tunes, CP5 and CUETP8M1. In the Figure 4.11, it is shown that there is a difference in the high pseudorapidity region for these two tunes and according to this comparison, the CUETP8M1 tune will provide better agreement with data. Figure 4.10: Data to simulation comparison of charged particle distributions: trans-verse momentum and pseudorapidity. Figure 4.11: Comparison of transverse momentum and pseudorapidity of charged particles distributions for CP5 and CUTEP8M1 tunes at generator level. 4.

5 Unfolding method In order to compare the obtained results with the theoretical predictions or with the results from the

70

have to be corrected for the effects coming from the detector impact itself. The detector

effects include the object reconstruction inefficiency inside of the acceptance of the detector and also the misidentification of the object of interest. In addition, since the reconstruction system has a finite resolution, the measured value of observable usually does not correspond to the truth one. To account for these effects the procedure called unfolding is performed. This procedure is based on MC simulation which can provide information about the measured and original values of the specific observable. The truth value, which is the result of the simulation procedure described in Section 1.4 will be referred to as generated observable, while the measured value after the detector simulation will be referred to as reconstructed observable. The reconstructed events have to pass the selections described in Section 4.3, which means that also generated events are selected in a specific phase space. Phase space The

phase space at the generator level is chosen to match the selections at the

37

82

reconstructed level. To take into account the effects of final state QED radiation of muons on measured observables, we used so called "dressed" muons. At the generator level, the photons that are inside of the cone  $\Delta R(I, \gamma) < 0.1$  around muons are merged with such muon. The merging is done such that the four-momentum of photons are added to the closest muon: pdµressed = pbµare + p $\gamma$ , (4.10)  $\Sigma \gamma$  where the term bare (dressed) corresponds to the lepton before (after) correction. Two dressed leptons with opposite charges and the largest transverse momentum are selected and required to have pT larger than 25 GeV (first muon) and 20 GeV (second muon). The leptons are

required to be within pseudorapidity region |  $\eta$ | < 2.4 and the invariant mass of leptons is required to be

113

within a certain interval. Unfolding procedure The relation between the reconstructed and generated observable can be defined as: m yi = Ai,jxj + bi,  $1 \le i \le n$  (4.11)  $\sum_{i=1}^{n} 1 \le n$ 

where the sum runs over the m bins of the generated distribution while the

204

number of bins at the reconstructed level is n. Aij represents the matrix of probabilities that describes the bin migration at the reconstructed level. The average expected value is yi. The background contribution for the specific bin is bi.

Unfolding procedure is done using the TUnfold package [88] where the estimation of the true value is done using the least square method with Tikhonov regularization [89]. By determining the stationary point in Langrangian, the statistical fluctuation of the expected value is amplified which causes fluctuation in x. To address these fluctuations regularization

is used. In the measurements presented in this thesis, the regularization is not used. Therefore, the unfolding procedure is performed by minimizing the following expression:  $\chi 2 = (y - Ax)T \ Vy - y1(y - Ax)$ . (4.12) The response matrices A, are obtained from the simulated signal sample. The example of the response matrices of the measured variables are shown in Figure 4.12. The vertical axis on the histogram corresponds to the generated variable, while on the horizontal axis the reconstructed level one is shown. On the histogram numbers represent the probability that generated level value is reconstructed as a specific value at the reconstructed level. The events that are used for determining the response matrix are the ones that pass the selection required for both reconstructed and generated levels. Figure 4.12: Response matrices for zero-jettiness (left) and one-jettiness (right). 4.6 Uncertainties

Two types of uncertainties are considered in the analysis: statistical uncertainties and systematic uncertainties. The statistical uncertainties are

coming from statis- tical limitation in measurement and from response matrices (unfolding statistics) which are estimated using the unfolding library. Systematic uncertainties include uncertainties from several different sources. Most of the systematical

uncertainties are estimated by varying the corresponding parameter up and down by one standard deviation

. The measurement is then performed with the modified parameter and the average of the

difference with respect to the central value is taken as the standard deviation of the measurement. Systematical uncertainties are added in

quadrature assuming each uncertainty is independent. Pileup The uncertainty of the pileup reweighting applied in simulation is obtained by vary- ing the minimum bias cross section by 4.7% up and down. The unfolding procedure is then performed for both new pileup profiles. Luminosity The uncertainty assigned to the luminosity is 2.5 % [90]. It

is applied on globally scaling to extract the cross section

127

and for normalization of background samples before subtracting from data Background The uncertainty in the estimation of background that is subtracted from data is determined by varying the cross section by the largest uncertainty in the cross sections used for normalization. This uncertainty corresponds to the tt process, it is 6% [82] and

takes into account PDF and scale uncertainties. The variation of cross section

113

is done before background substraction. Lepton

**Energy Scale The uncertainty** in the **energy scale** of muons **is estimated from the**Rochester corrections **uncertainties. The** 

59

uncertainty includes the statistical component and the un-certainties accounted for the fitting method used (fitting function, Z mass window). These uncertainties are added in quadrature and used for varying the Rochester correction up and down. Lepton Energy Resolution The uncertainty of the lepton energy reconstruction is estimated in the signal sam- ples by smearing the lepton by 0.6 % with respect to the corresponding lepton at the generated level. Lepton reconstruction and trigger efficiency The reconstruction and trigger efficiency is estimated

by varying the corresponding scale factors up and down by one standard deviation. For identification and

102

isolation scale factors the considered uncertainties are statistical. Trigger scale factors include both statistical and systematical uncertainties as explained in Section 4.4. Track pT The uncertainty of the track pT is estimated for each track of each event. It is propagated analytically to track based variables assuming uncorrelated Gaussian uncertainties. The uncertainty on the reconstruction-level data distribution is de-rived from this event-by-event uncertainty with a toy Monte-Carlo using 100 replicas. The unfolding matrix is used to derive the uncertainty on the measured differential cross-sections, following the same method as the one used to propagate the data statistical uncertainties. Track efficiency The uncertainty of the track reconstruction efficiency is estimated by varying the measured variable by 2.3% in the low pT region (less than 20 GeV) and 1% in the 100 higher pT region. The 2.3% and 1% uncertainties are estimated for charged pions [91] and muons [92]. Unfolding model The uncertainty of the unfolding model is estimated by reweighting the signal sim- ulation to match the data

# and using it as an alternative model for the unfolding. The

40

weights are obtained from the ratios fine binned histograms of background- subtracted data to the signal. The ratios are fitted with the polynomials to smooth out statistical fluctuations. The example of one of the fits is show in Figure 4.13. The results of the fits are used for obtaining weights for each event. After reweight- ing, new response matrix is generated and used for unfolding. The

difference with respect to the central value is taken as the uncertainty Figure 4.13: The

130

fit function used for reweighting one-jettiness 4.6.1 Theoretical predictions uncertainties The measured cross sections are compared with three different theoretical descrip- tions MadGraph5\_amc@nlo (MadGraph) at next-to-leading order (NLO), Mad- Graph at leading order (LO), and Geneva described in Section 1.4. The statistical uncertainties originating from MC sample statistics are estimated for these predic- tions. In addition, the uncertainties in ME calculations are estimated forMadGraph NLO and Geneva. For MadGraph NLO sample, the uncertainty originating

from missing terms in the fixed-order calculation is obtained by varying the renormalization [134] (  $\mu$ R) and factorization scales (  $\mu$ F) by factors 0.5 , 1 and 2. The envelope of the

variation is considered as uncertainty, with the excluded cases where the scales are varied in the opposite direction. The uncertainty in the extraction of the PDF set

is estimated using the 100 replicas of NNPDF 3.0 NLO, where the

112

standard deviation is taken as uncertainty. The uncertainty in  $\alpha S$  is estimated by variation of the scale by its uncertainty (0.001) up and down. The theoretical variations in the Geneva sample are estimated using the 7- fold variation of the renormalization and factorization scale and for variation of the scales used for resummation [93].

For each event the calculation of its cross section with a different set of profile scales

131

is performed and the corresponding weights are produced for each event. The profile variations include variation up and down of the scales and variation of transition points by 0.05. The maximum ± absolute deviation from the central value among these six profiles is considered as the ressumation uncertainty and

by adding the fixed order uncertainty the total perturbative uncertainty is obtained

203

. 4.7 Results The cross sections obtained after background subtraction and unfolding procedures are computed and compared to theoretical prediction described in Section 1.4. For the results obtained in the Z peak region, 76 < mll < 106 GeV, the dominant source of uncertainty is the unfolding model. With the alternative model for unfold- ing, the uncertainty goes to 15% for the lowest values of the track based variables. The second largest contribution to the total uncertainty comes from track efficiency uncertainty. The uncertainty breakdown plots for zero-jettiness and one-jettiness are shown in Figure 4.14. Due to the large uncertainties that are coming from the unfolding model itself,

besides the unfolded results, the distributions at the detector level are shown for all variables. For the detector level distribution, the uncertainties include only sta- tistical uncertainty coming from data. The background samples are included in the detector level distribution but have small contribution in the region of Z peak, therefore they are not visible in the plots shown with linear scale. Figure 4.14: Uncertainty breakdown for zero-jettiness and one-jettiness The measured cross sections as a function of zero-jettiness and the distribution at detector level are shown in Figure 4.15. At the low zero-jettiness the NNLL Geneva gives better description than NLO and LO MadGraph. For the high zero-jettiness, all three predicitions show fair agreement with the measurement. The difference in the peak region between data and simulation can be caused by the different modeling of multiple parton interaction in simulation. The sensitivity of zero-jettiness on MPI is shown in Figure 4.16. Using the samples generated with Geneva and showered with pythia8, zero-jettiness is computed in the Z peak region with and without MPI modeling included.

It can be seen that the MPI affects the shape of the distribution

200

especially in the peak region. For MadGraph and Geneva, different pythia8 tunes were used, CP5 and CUETP8M1 respectively. Figure 4.15: Data to simulation comparison and the differential cross section as a function of zero-jettiness. Figure 4.16: The distribution of zero-jettiness computed for the events without MPI (left) and with MPI (right).

The measured cross section as a function of zero-jettiness and the

3

detector level comparison of zero-jettiness distribution in different pT (Z) bins are presented in Figure 4.17 - Figure 4.20. The four regions observed are : pT (Z) < 6 GeV, 6 < pT (Z) < 12 GeV, 12 < pT (Z) < 25 GeV and pT (Z) > 25 GeV. 104 In the lowest pT (Z) region, it is expected to have low jet activity from primary collision and it expected to be particularly sensitive to UE characteristics. In this region none of the generators describe successfully the data. NLO and LO Mad-Graph overestimates data while Geneva underestimates the measurements. In the regions with pT (Z) 6-12 GeV and 12-25 GeV, the better description of data by predictions is observed. In the region with pT (Z) > 25 GeV, where it is expected to have at least one jet with high transverse momentum, there is still a significant difference in the MC generators with respect to the measurement. In this region NLO MAdGraph describes measurement better than other two generators. While LO MadGraph underestimates data, Geneva prediction overestimated data on the whole range. Figure 4.17: Data to simulation comparison and the differential cross section as a function of zero-jettiness for pT (Z) < 6 GeV. 105 Figure 4.18: Data to simulation comparison and the differential cross section as a function of zero-jettiness for < pT (Z) < 12 GeV. 6 Figure 4.19: Data to simulation comparison and the differential cross section as a function of zero-jettiness for 12 < pT (Z) < 25 GeV. 106 Figure 4.20: Data to simulation comparison and the differential cross section as a function of zero-jettiness for pT (Z) > 25 GeV. The zero-jettiness, one-jettiness and the sum of the transverse momentum of particles are measured in the three additional invariant mass bins: 125 < mll < 150 GeV, 150 < mll 350 GeV and 350 < mll < 1500 GeV. The measured cross section as a function of zero-jettiness and the detector level comparison of zerojettiness distribution in different mll bins are presented in Figure 4.21 - Figure 4.23. From the detector level distributions, it can be seen that as going higher in the invariant mass regions, the contributing of background becomes significant. In particular, the contribution of the background coming from the tt process. In the invariant mass bin 125-150 GeV the

Geneva prediction describes the data better than other predictions. At the low zero-jettiness, NLO and LO MadGraoh overestimated data. As going towards higher invariant mass bin, the description of data by MadGraph improves. The dominant uncertainty source as going to the higher mass bins is originating from the statistical limitations of data and simulation. Figure 4.21: Data to simulation comparison and the differential cross section as a function of zero-jettiness for 125 < MII < 150 GeV. Figure 4.22: Data to simulation comparison and the differential cross section as a function of zero-jettiness for 150 < MII < 350 GeV. 108 Figure 4.23: Data to simulation comparison and the differential cross section as a function of zero-jettiness for 350 < MII < 1500 GeV. The measured cross sections as a function of one-jettiness and the distribution at detector level are shown in Figure 4.24. Similarly to the zero-jettiness, low zero-jettiness region is better described by Geneva than NLO and LO MadGraph. For the higher one-jettiness, all three predicitions show fair agreement with the measurement. Figure 4.24: Data to simulation comparison and the

differential cross section as a function of one-jettiness. The measured cross section as a function of zero-jettiness and the

detector level comparison of zero-jettiness distribution in different pT(Z) bins are presented in Figure 4.25 - Figure 4.28. Unlike zero-jettiness, one-jettiness in not measured in the bin where pT(Z) is lower than 6 GeV. In this region a high energy jet is emitted with rather low probability and the distribution would be misleading. The four regions where onejettiness is observed are: 6 < pT(Z) < 12 GeV, 12 < pT(Z) < 25 GeV, 25 < pT(Z) < 35 GeV and pT(Z) > 35 GeV. In the lowest pT(Z), none of prediction describes well data. At the low one- jettiness, all the prediction overestimate data. For the higher pT(Z), data is better described at the high one-jettiness compared with the pT(Z) 6-12 GeV. In the re-gion pT(Z) > 35 GeV, LO MadGraph describes rather well the data, while NLO MadGraph and Geneva show disagreement, especially at the low one-jettiness. Figure 4.25: Data to simulation comparison and the differential cross section as a function of one-jettiness for < pT (Z) < 12 GeV. 6 Figure 4.26: Data to simulation comparison and the differential cross section as a Figure 4.27: Data to simulation comparison and the differential cross section as a function of one-jettiness for 25 < pT (Z) < 35 GeV. Figure 4.28: Data to simulation comparison and the differential cross section as a function of one-jettiness for pT (Z) > 35 GeV. The measured cross section as a function of zero-jettiness and the detector level comparison of one-jettiness distribution in different mll bins are presented in Figure ?? - Figure 4.39. The large uncertainties, especially at the high one-jettiness are originating from the statistical limitation of data and simulation. For the mass bin mll in range 125-150 GeV Geneva shows fair agreement with data. NLO and LO MadGraph overestimates data at the low one-jettiness region. In the higer invariant mass bins, all the predictions show rather well. Figure 4.29: Data to simulation comparison and the differential cross section as a Figure 4.30: Data to simulation comparison and the differential cross section as a function of one-jettiness for 150 < MII < 350 GeV. Figure 4.31: Data to simulation comparison and the differential cross section as a function of one-jettiness for 350 < Mll < 1500 GeV. The measured

cross sections as a function of the sum of the transverse momentum of particles and the distribution at detector level are shown in Figure

4.32. At the low pT,sum region, none of the predictions describes well data, while at the higher pT,sum there is a good
agreement with data observed for all the predictions. Figure 4.32: Data to simulation comparison and the
differential cross section as a function of the sum of the transverse momentum of charged particles The measurement of the
sum of transverse momentum of particles are also per- formed in four different $pT(Z)$ bins: $pT(Z) < 6$ GeV, $6 < pT(Z) < 12$ GeV, $12 < pT(Z) < 25$ GeV and $pT(Z) > 25$ GeV. The measured
cross section as a function of pT ,sum and the detector level comparison of pT,sum 211 distribution in
different $pT(Z)$ bins are presented in Figure 4.33 - Figure 4.36. In the region with the lowest $pT(Z)$ none of the predictions describe well the data. As going towards the higher $pT(Z)$ regions, where it is expected to have higher jet activity, the predictions are doing better in describing the data. In the region where $pT(Z)$ is higher than 25 GeV, MadGraph is describing data better than other predictions. Figure 4.33: Data to simulation comparison and the
differential cross section as a function of the sum of the transverse momentum of charged particles for pT ( Z
) < 6 GeV. Figure 4.34: Data to simulation comparison and
the differential cross section as a function of the sum of the transverse momentum of
charged particles $6 < pT(Z) < 12$ GeV. Figure 4.35: Data to simulation comparison and the
differential cross section as a function of the sum of the transverse momentum of charged particles for 12 < pT ( Z
) < 25 GeV. Figure 4.36: Data to simulation comparison and the
differential cross section as a function of the sum of the transverse momentum of charged 5 particles for pT ( Z

) > 25 GeV. The measured cross section as a function of pT,sum and the detector level com- parison of pT,sum distribution in different mll bins are presented in Figure 4.37 - Figure 4.39. The large uncertainties, especially at the low pT,sum region have big contribution from data and MC statistical uncertainties. In the region where invariant mass is in range 125-150 GeV all the prediction describe well data whithin the uncertainty. For the higher mass bins, the data is underestimated by the LO Madraph and Geneva. Figure 4.37: Data to simulation comparison and the

differential cross section as a function of the sum of the transverse momentum of charged particles for

125 < MII < 150 GeV. Figure 4.38: Data to simulation comparison and the

differential cross section as a function of the sum of the transverse momentum of charged particles for

150 < MII < 350 GeV. Figure 4.39: Data to simulation comparison and the

differential cross section as a function of the sum of the transverse momentum of charged particles for

350 < MII < 1500 GeV. Chapter 5 Measurement of jet-based event shape observables In this chapter, the measurements of jet based event shape observables in the pro- duction of the Z boson with the association of jets are presented. These observables are measured in the events with real Z boson, where invariant mass of leptons is from 76 to 106 GeV. The definition of the jet based observables in presented in the in Section 5.1. The data samples and simulation are the same as defined in Section 4.2. In addition, the corrections for jets and criteria for selecting

events with a Z boson and one or more jets

produced are presented in Section 5.2. For obtaining the result, the TUnfold method is used, and additional uncertainties related to jets that are considered are defined in

Section 5 .3. The final results are presented in Section 5 .4. 5.1

Observable definition The vetoes on the hadronic activity are used for classifying events with the minimum number of jets (inclusive) or with the exact number of jets (exclusive) to suppress background or to increase sensitivity for a

particular process of interest. To select the events based on their jet multiplicity, the usual requirement is to have a specific number of jets with the transverse momentum above some threshold. Besides the transverse momentum, additional variables can be used for selection as defined in [4]. These variables depend on the jet transverse momentum pjT and weighting function of the jet rapidity  $f(yi): \tau j = pjT f(yi)$  Two different weighting function are considered: (5.1)  $\tau B: f(yi) = e^{-|yj-Y|} \tau C: f(yi) = 1 2 \cosh(yj - Y)$  (5.2) where Y is the rapidity of the dimuon system. The weighting functions are decreasing functions of the absolute jet rapidity. Therefore the small values of  $\tau j$  are obtained either for small values of transverse momentum or for large values of absolute rapidity. In figure 5.1 the weighting functions are shown.

It can be seen that for high values of |yi| the

119

 $\tau B$  and  $\tau C$  are equivalent while for rapidity around 0,  $\tau C$  is smoother than  $\tau B$ . Using  $\tau B$  and  $\tau C$  for event selection allows to have a constrain which is tight at central rapidity and it gets looser for the forward rapidity. This type of selection is convenient for processes that have jets well separated in rapidity, such as the Vector Boson Fusion process. Figure 5.1: Rapidity weighting functions for  $\tau B$ ,  $\tau C$ , and pT Compared to the  $\tau B$ ,  $\tau C$  variable has an experimental advantage that can be measured to the smaller values which is why I decided to measure this variable. The differential cross section is measured for two different variablees derived from previous definitions:  $\tau C$  j = max mT 1 J (2 cosh(yj - Y)) (5.3)  $\tau C$  j = mT  $\tau C$  j

between entities i and j (dij) and distance between the beam and entity i

72

(diB): dij = min(kt2ip, k2tjp)  $\Delta$ Ri22j (5.4) diB = kt2ip, where  $\Delta$ 

 $2ij = (yi - yj)2 + (\phi i - \phi j)2$  and kti, yi and  $\phi i$  are transverse momentum, rapidity and azumuthal angle of the entity i. R is the radius parameter that determines the size of the

12

jet and p is the parameter that sets the relative power of the energy with respect to the geometrical scales. For the jets used in

137

this analysis, the radius parameter is set to 0.4

137

and for anti-kt jets, p is set to 1. The jet clustering algorithm then determines the minimum of the two distances defined. If dij

is the minimum, the entries i and j are combined into one entry by summing of their 97 four

-momentum.

If diB is the minimum, i is considered to be the final jet. The

145

clustering process is repeated over all entries. The jet reconstruction is affected by the particles that are coming from the pileup. In order to mitigate the pileup events the technics such as Charged Hadron Substraction (CHS) [55] or Pileup Per Particle Identification (PUPPI) [95] can be used. CHS algorithm uses the information from the tracking system to identify particles that are originating from pileup vertex. These charged particles are then removed, and the remaining charged particles and all neutral particles are kept and used for jet reconstruction. PUPPI algorithm considers the particle level candidates and assign

a weight in the range from 0 to 1 for each particle , where the value 1 is assigned to the

128

particles that are coming from the primary vertex while those particles originating from pileup have the weight 0. For the charged particles, weight assignment is based on the information from the tracking system. Charged particles that are

used in the fit of the primary vertex are assigned with weight 1, while the charged particles associated with the pileup vertex are assigned with weight

0. The weights for neutral particles are assigned based on the discriminating variable  $\alpha$ :  $\alpha = \log pT$ ,  $j \neq j$ ,  $\Delta R$  ( $\Delta R$ ), (5.5) where the sum

runs over particles j in the cone with radius 0.4 of

14

is the transverse momentum of particle j and  $\Delta Rij$  is the distance between the particles 78 i and j

in the  $\eta$   $\phi$  frame. In the region with  $|\eta|$  < 2.5, j are charged – particles from the primary vertex and in region  $|\eta|$  > 2.5 j are all the reconstructed particles. The  $\alpha$ i value of neutral particles

is compared with median  $\;(\alpha PU\,)\;\;$  and RMS  $\;\;(\alpha RPMUS)\;\;$  of a distribution  $\;$  obtained for charged particles

from pileup, using a signed  $\chi 2$  approximation: signed  $\chi 2 = (\alpha i - \alpha P U) | \alpha i - \alpha P U |$ . ( $\alpha RPMU S$ ) 2 (5.6) The neutral particles for which the value of signed  $\chi 2$  is large are most likely originating from the primary vertex. The final weights for neutral particles are computed with a

cumulative distribution function of the  $\chi 2$  with one degree of freedom

94

94

: wi = F $\chi$ 2,NDF=1(signed $\chi$ 2). (5.7) The obtained weights are used for rescaling the four momentum of particles which helps in reducing the pileup contribution. In order to account for inefficiencies, nonlinearlities and finite resolution in energy and position of the reconstructed jets, the

jet energy corrections (JEC) derived from simulation is applied for both CHS and PUPPI

94

jets. In addition,

since the jet energy resolution is different in data and simulation, the smearing

149

of the jets is performed. The four-momentum of a

reconstructed jet is rescaled with the factor: CJER = 1 + (SJER - 1) pT - pgTen , ( 5 173 8) pT where

is the transverse momentum of reconstructed jet , pgTen is the transverse momentum of the corresponding jet at generator level and SJER is the data-to- simulation core resolution scale factor. If

the corresponding generator level jets are not found, stochastic smearing is performed. The correction factor, in that case, is computed as: CJER =  $1 + N (0, \sigma JER) \max(s2JER - 1, 0), (5.9)$  where

 $\sigma$ JER is the relative pT resolution in simulation and N (0 ,  $\sigma$ ) is the random  $\sqrt{n}$  number 153 from the normal distribution with

a zero man and variance  $\sigma$ 2. In order to decide which jet algorithm to use, the studies on performance of these two methods, CHS and PUPPI, are performed. In the following, jets

are required to be within the pseudorapidity range of  $|\eta| < 2$  .5 and to have

\_\_\_

9

17

at least one jet with the transverse momentum above 20 GeV. In order to avoid misidentification and to reject the noise, the identification selection summarized in Table 5.1 is used. Variable Selection

Charged Hadron Function > 0 Charged Hadron Multiplicity > 0 Charged EM Fraction < 0 .80 3

Neutral Hadron Fraction < 0 .90 Neutral EM Fraction < 0

.90 Muon Fraction < 0.80 Table 5.1: Criteria for identification of jets. In addition, the jets are required to be separated from the muons by selecting only the jets with  $\Delta R$ (jet, lepton) > 0.4. In Figure 5.2, the distribution of the leading jet transverse momentum is shown at generator level and at reconstructed level for both CHS and PUPPI jets. For the pT above 30 GeV, both CHS and PUPPI jets show good performance. For the lower jet transverse momentum (from 20 to 30 GeV), better performance is observed for PUPPI jets. Figure 5.2: Comparison of the leading jet transverse momentum distribution at generated level, reconstructed level with CHS and reconstructed level with PUPPI algorithm. To see the performance of pileup identification, the ratio of pileup jets to geniune jets is studied. The jets are classified according to the

the difference between the azimuthal angle  $\phi$  of the leading jet and the

19

are required to have  $\Delta \phi(Z, jet) < 1.5$ , while

94

non pileup jets have  $\Delta \phi(Z, jet) < 2.5$ . In Figure it can be seen that CHS jets have

a strong dependence on the number of vertices in detector

94

, especially for the events where it is required to have leading jet with transverse momentum higher than 10 GeV and 20 GeV. PUPPI shows a stable behavior even for the leading jet pT of 20 GeV. Since for measuring jet based event shape variables, it is important to go as low as possible in pT, we decided to use PUPPI jets and to use events where at least one jet with transverse momentum above 20 GeV.

Figure 5.3: Data to simulation comparison of the leading jet transverse momentum and

55

inclusive number of jets. After the

sleections and corrections applied, the comparison of the number of reconstructed jets and of the

transverse momentum of the leading jet from the event in data and

67

55

simulation is shown in Figure 5.4. It can be seen that there is a 10% difference between data and simulation in the distributions of the jet transverse momentum.

Figure 5 .4: Data to simulation comparison of the leading jet transverse momentum

and inclusive number of

jets. 5.3 Uncertainties In addition to the uncertainties defined in Section 4.6, the uncertainty is assigned also for the jet energy scale and jet energy resolution.

Jet energy scale The uncertainty on the jet energy scale is estimated by scaling the

127

t momentum in data by the uncertainties that are common for

all CMS analyses []. These factors are pT and  $\eta$  dependent. Jet energy resolution The uncertainties for the resolution of jets are determined by varying the smearing factor used in simulation by their uncertainty. 5.4 Results The jet based variables are measured for the events with the production of real boson in invariant mass range of 76 < mll < 106 GeV. For the jet based variables, the main source of uncertinty comes from the jet energy correction and jet energy scale. For the low  $\tau$  max and  $\tau$  sum region, these uncertianties go up to %. The uncertainties backgrund plots are shown in Figure 5.5. Figure 5.5: Uncertainty breakdown for  $\tau$  max and  $\tau$  sum The measured cross section as a function of  $\tau$  max and the detector level compari- son of  $\tau$  max distribution are shown in Figure 5.6. At the low  $\tau$  max the best generator for describing the measurement is NLO MadGraph. In the peak region of the dis-tribution Geneva overestimates the data while at the high  $\tau$  max NLO MadGraph and Geneva show good agreement with data and LO MadGraph underestimates data. The different tunes used for MadGraph and for Geneva can contribute to the differences observed in the distributions [32]. The measured cross section as a function of  $\tau$  sum and the detector level comparison of  $\tau$  sum distribution are shown in Figure 5.7. Low  $\tau$  sum region is best described by the LO MadGraph. Both NLO MadGraph and Geneva overestimate data. At high  $\tau$  sum, NLO MadGraph gives the best description of data, while LO Mad-Graph and Geneva predicts fewer events in this region. Figure 5.6: Data to simulation comparison and the

differential cross section as a function of Tmax . 130 Figure 5. 7 : Data to simulation 21 comparison and the differential cross

section as a function of  $\tau$ sum . Conclusion I have presented in this thesis the work I have performed during my PhD. It has been carried out within the CMS experiment collaboration. The main focus has been on the measurement of N-jettiness variables in production of Z boson with association with jets presented in Chapter 5 and measurement of jet based event shape variables presented in Chapter 6. One part of the thesis is devoted to intercalibration and perfromance studies of the CMS electromagnetic calorimeter which is described in Chapter 3. The excellent resolution of the CMS electromagnetic calorimeter plays an im-portant role in many physics analysis performed at CMS. In particular, its precise measurement of electron and photon energy had a big contribution in discovery of Higgs boson through the H  $\rightarrow \gamma\gamma$  channel during LHC Run 1 period. Run 2 data taking period, with the increased pileup and radiation level, created challenging en- vironment for ECAL. In order to optimize performance the calibration of relative response of the ECAL channels and corrections for the response variation in time are performed. My work included delivering the intercalibration constants using the Z  $\rightarrow$  ee method. The intercalibration constants were derived for all three years of Run 2 data-taking period. The constant monitoring and calibration resulted in excellent performance of ECAL during Run 2. The energy resolution

for electrons from Z-boson decays was at the level of 1.7% in the low pseudorapidity region

4

. It was also shown that the

ageing of the detector and much higher instantaneous luminosity. The second part of my work has been the

measurement of the differential cross section of Z boson production in association with jets in proton-proton collisions at 13 TeV has been presented. The data recorded by the CMS detector during 2018, corresponding to the integrated luminosity of

59.4 fb1,

has been analysed. The mea-surements of Z boson in association with jets processes are crucial for understanding and

3

3

modeling QCD interactions. In addition, this processes

is an important back- ground for many Standard Model processes and for the processes 112 beyond the SM . Therefore, precise knowledge of

Z boson production in association with jets has great importance for exploiting the potential of the LHC experiments. The

differential cross section has been measured as a function of

147

track based event shape variables and as a function of jet based event shape variables. The measurements

have been compared with three types of theoretical predictions with LO, NLO and NNLO 3

QCD accuracies obtained with two MC generators , Mad-Graph5\_ amc

@nlo and Geneva. Track based variables that have been measured are the zero-jettiness, one-jettiness and sum of the transverse momentum of charged particles. These variables can be used as a veto for hard radiation or jets and to define a theoretically well-controlled exclusive N-jet cross section. Track based variables are very sensitive to the underly- ing events and soft radiation, therefore studies of these variables give valuable input for Monte Carlo generators developments. The measurements are performed for the events with pairs of muons produced in the decay of

off shell Z boson with invariant mass between 125 and 150 GeV, 150 to 350 GeV and 350 and 1500 GeV. Track based variables are also measured in four different Z boson transverse momentum regions. The measurements done for the real Z boson showed that among the predictions the Geneva describes the data best, especially at the low region of the measured variable. For the zero-jettiness, there is a good description of data in inclusive case. The low Z boson transverse momentum region is described best by the Geneva generator, whille at high Z boson transverse momentum, where we expect to have one or more jets accompanying the Z boson, Geneva does not describe the data well. In that region, NLO MadGraph5\_amc@nlo is doing best for all measured variables. For one-jettiness, no prediction is satisfactory. For the higher invariant mass regions, all predictions show fair agreement with the data. Measurements of these variables showed good potential for studies of underlying events. By studying track based variables for the invariant mass above the Z peak, the regime similar of Higgs boson has been explored. Jet based variables that are measured are tmax and tsum. These variables are defined using jet transverse momentum weighted by a rapidity dependent function. Jet based variable introduce a possibility to apply tight veto on central jets while at forward rapidities the veto constrain gets looser. The measured variables showed good agreement with the prediction, especially with the MadGraph5\_amc@nlo. The measurements performed show good potential for testing resummation. Us- ing Njettiness variables as a jet veto in order to have a better control on theory uncertainty, would require to understand better the predictions including resumma- tion of zero-jettiness like the one obtained with Geneva. Bibliography [1] CMS Collaboration. Observation of a new boson at a mass of 125 GeV with the CMS experiment at the LHC. [2] ATLAS Collaboration. Observation of a new particle in the search for the Standard Model Higgs boson with the ATLAS detector at the LHC. Phys. Lett. B, 716:1-29, 2012. doi:10.1016/j.physletb.2012.08.020. [3] I. W. Stewart, F. J. Tackmann, and W. J. Waalewijn. N jettiness: an in-clusive event shape to veto jets. Physical review letters, 105(9):092002, 2010. doi:10.1103/PhysRevLett.105.092002. [4] S. Gangal, M. Stahlhofen, and F. J. Tackmann. Rapidity-dependent jet vetoes. Physical Review D, 91(5), Mar 2015. doi:10.1103/physrevd.91.054023. [5] D. Galbraith. Standard Model of the Standard Model. Last accessed October 2021 http://www.who.int/mediacentre/factsheets/fs282/fr. [6] Paul AM Dirac. Theory of electrons and positrons. Nobel Lecture, 12:320–325, 1933. [7] S. L. Glashow. Partial-symmetries of weak interactions. Nuclear physics, 22(4):579–588, 1961. [8] S. Weinberg. A model of leptons. Physical review letters, 19(21):1264, 1967. [9] A. Salam. Weak and electromagnetic interactions. In Selected Papers Of Abdus Salam: (With Commentary), pages 244–254. World Scientific, 1994. 135 [10] Peter W Higgs. Broken symmetries and the masses of gauge bosons. Physical Review Letters, 13(16):508, 1964. [11] F. Englert and R. Brout. Broken symmetry and the mass of gauge vector mesons. Physical Review Letters, 13(9):321, 1964. [12] J. Ellis. Higgs physics. 2013. arXiv preprint arXiv:1312.5672. [13] Particle Data Group. W boson mass. https://pdg.lbl.gov/2020/listings/ rpp2020-list-w-boson.pdf. [14] Particle Data Group. Z boson mass. https://pdg.lbl.gov/2020/listings/ rpp2020-list-z-boson.pdf. [15] P. J. E. Peebles and B. Ratra. The cosmological constant and dark energy. Reviews of modern physics, 75(2):559, 2003. doi:10.1103/RevModPhys.75.559. [16] Richard P. Feynman. Very high-energy collisions of hadrons. Phys. Rev. Lett., 23:1415-1417, 1969. doi:10.1103/PhysRevLett.23.1415. [17] R. K. Ellis, W. J. Stirling, and B. R. Webber. QCD and collider physics. Cambridge university press, 2003. [18] F. D. Aaron et al. Inclusive Deep Inelastic Scattering at High Q2 with Longitudinally Polarised Lepton Beams at HERA. JHEP, 09:061, 2012. doi:10.1007/JHEP09(2012)061. [19] H. Abramowicz et al. Measurement of

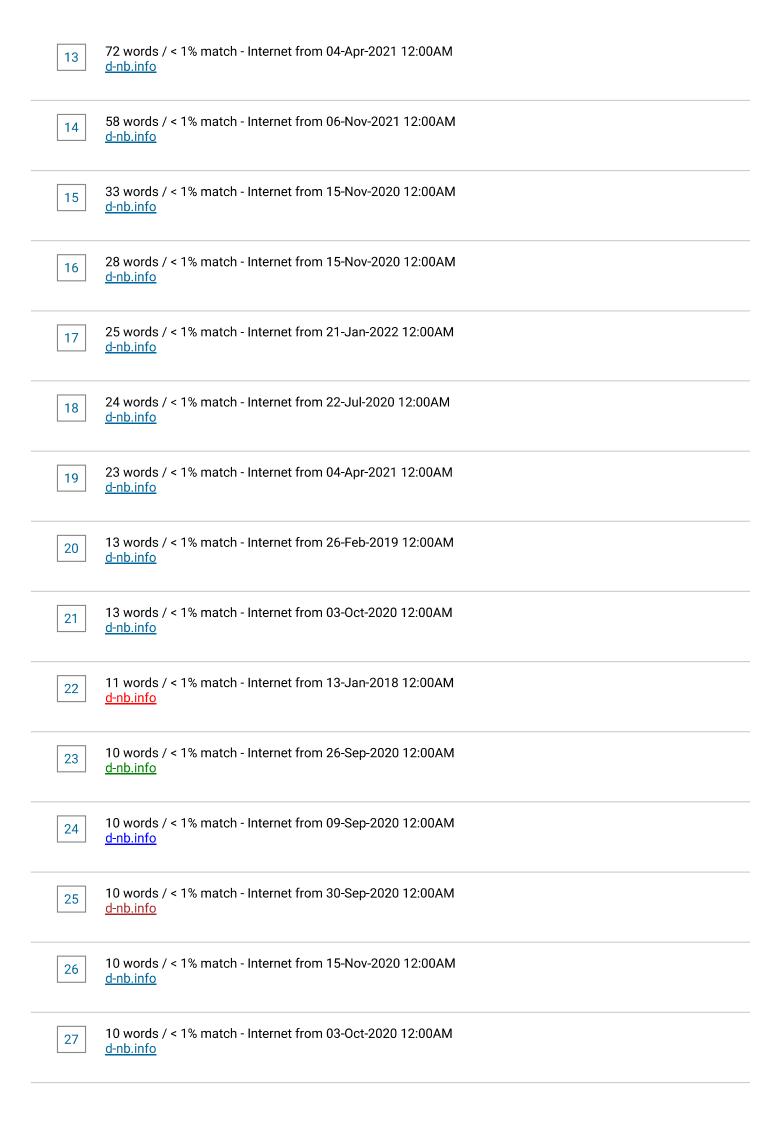
high-Q2 neutral current deep inelastic e+p scattering cross sections with a longitudinally polarized positron beam at HERA. Phys. Rev. D, 87(5):052014, 2013. doi:10.1103/PhysRevD.87.052014. [20] Y. L. Dokshitzer. Calculation of the structure functions for deep inelastic scat-tering and e+e- annihilation by perturbation theory in quantum chromodynamics. Zh. Eksp. Teor. Fiz, 73:1216, 1977. [21] V. N. Gribov and L. N. Lipatov. Deep inelastic e p scattering in perturbation theory. Technical report. [22] G. Altarelli and G. Parisi. Asymptotic freedom in parton language. Nuclear Physics B, 126(2):298-318, 1977. doi:10.1016/0550-3213(77)90384-4. [23] A. Buckley, J. Ferrando, S. Lloyd, K. Nordström, B. Page, M. Rüfenacht, M. Schönherr, and G. Watt. LHAPDF6: parton density access in the LHC precision era. The European Physical Journal C, 75(3):1-20, 2015. doi:10.1140/ep jc/s10052-015-3318-8. [24] Richard D. Ball et al. Parton distributions from high-precision collider data. The European Physical Journal C, 77(10):1-75, 2017. doi:10.1140/epic/s10052-017-5199-5. [25] S. D. Drell and Tung-Mow Yan. Massive lepton-pair production in hadronhadron collisions at high energies. Physical Review Letters, 25(5):316, 1970. doi:10.1103/PhysRevLett.25.316. [26] N. Metropolis and S. Ulam. The Monte Carlo method. Journal of the American statistical association, 44(247):335-341, 1949. [27] T. Gleisberg, S. Hoeche, F. Krauss, A. Schälicke, S. Schumann, and J. Winter. SHERPA 1. α, a proof-of-concept version. Journal of High Energy Physics, 2004(02):056, 2004. doi:10.1088/1126-6708/2004/02/056. [28] S. Agostinelli et al. GEANT4-a simulation toolkit. Nuclear instru-ments and methods in physics research section At, 506(3):250-303, 2003. doi:10.1016/S0168-9002(03)01368-8. [29] R. Frederix and S. Frixione. Merging meets matching in MC@NLO. Journal of High Energy Physics, 2012(12):061, 2012. doi:10.1007/JHEP12(2012)061. [30] J. Alwall, R. Frederix, S. Frixione, V. Hirschi, F. Maltoni, O. Mattelaer, H.S. Shao, T. Stelzer, P. Torrielli, and M. Zaro. The automated computation of tree-level and next-to-leading order differential cross sections, and their matching to parton shower simulations. Journal of High Energy Physics, 2014(7):1–157, 2014. [31] J. Alwall et al. Comparative study of various algorithms for the merging of par- ton showers and matrix elements in hadronic collisions. The European Physical Journal C, 53(3):473-500, Dec 2007. doi:10.1140/epjc/s10052-007-0490-5. [32] A. M. Sirunyan et al. Extraction and validation of a new set of CMS Pythia 8 tunes from underlying-event measurements. The European Physical Journal C, 80(1):4, 2020. doi:10.1140/epjc/s10052-019-7499-4. [33] C. W. Bauer, F. J. Tackmann, and J. Thaler. GenEvA (I): A new frame- work for event generation. Journal of High Energy Physics, 2008(12):010, 2008. doi:10.1088/1126-6708/2008/12/010. [34] C. W. Bauer, F. J. Tackmann, and J. Thaler. GenEvA (II): A phase space generator from a reweighted parton shower. Journal of High Energy Physics, 2008(12):011, 2008. doi:10.1088/1126-6708/2008/12/011. [35] CMS Collaboration. Event generator tunes obtained from underlying event and multiparton scattering measurements. The European Physical Journal C, 76(3):1-52, 2016. doi:10.1140/epjc/s10052-016-3988-x. [36] L. Evans and P. Bryant. LHC machine. Journal of instrumentation, 3(08):S08001, 2008. doi:10.1088/1748-0221/3/08/S08001. [37] Roland E. Allen. The Higgs Bridge. Physica Scripta, 89(1):018001, 2013. doi:10.1088/0031-8949/89/01/018001. [38] E. Mobs. The CERN accelerator complex-August 2018. Technical report, 2018. http://cds.cern.ch/record/2636343. [39] CMS Collaboration. The CMS experiment at the CERN LHC. Journal of instrumentation, 3:S08004, 2008. doi:10.1088/1748-0221/3/08/S08004. [40] ATLAS Collaboration. The ATLAS experiment at the CERN Large Hadron Collider. Journal of instrumentation, 3:S08003, 2008. doi:10.1088/1748-0221/3/08/S08003. [41] LHCb collaboration. The LHCb detector at the LHC. Journal of instrumenta-tion, 3(08):S08005, 2008. doi:10.1088/1748-0221/3/08/S08005. [42] ALICE collaboration. The ALICE experiment at the CERN LHC. A Large Ion Collider Experiment. Journal of instrumentation, 3:S08002. doi:10.1088/1748-0221/3/08/S08002. [43] CMS Collaboration. Public luminosity results. https://twiki.cern.ch/ twiki/bin/view/CMSPublic/LumiPublicResults. [44] HiLumi Collaboration. The HL-LHC project. https://hilumilhc.web.cern. ch/content/hl-lhc-project. [45] T. Sakuma. Cutaway diagrams of CMS detector. In J. Phys.:

Conf. Ser. 513 022032, number CMS-OUTREACH-2019-001, 2019. [46] CMS Collaboration. The CMS magnet project: Technical Design Report. Technical design report. CMS. CERN, Geneva, 1997. https://cds.cern.ch/ record/331056. [47] CMS collaboration. Precise mapping of the magnetic field in the CMS barrel yoke using cosmic rays. Journal of Instrumentation, 5(03):T03021, 2010. [48] CMS collaboration. The CMS tracker system project: Technical Design Report. Technical report, CMS-TDR-005, 1997. [49] CMS collaboration. The CMS tracker: addendum to the Technical Design Report. Technical report, CERN-LHCC-2000-016, 2000. [50] CMS collaboration. Description and performance of track and primary- vertex reconstruction with the CMS tracker. Journal of Instrumentation, 9(10):P10009, 2014. [51] CMS collaboration. CMS technical design report for the pixel detector upgrade. Technical report, Fermi National Accelerator Lab.(FNAL), Batavia, IL (United States), 2012. doi:10.2172/1151650. [52] CMS Collaboration. Overview of the CMS electromagnetic calorimeter. Nucl. Phys. B Proc. Suppl., 78:186-191, 1999. doi:10.1016/S0920-5632(99)00544-7. [53] CMS Collaboration. Studies of the response of the prototype CMS hadron calorimeter, including magnetic field effects, to pion, electron, and muon beams. Nuclear Instruments and Methods in Physics Research Section A, 457(1-2):75-100, 2001. [54] CMS Collaboration. The CMS muon project: Technical Design Report. Techni- cal design report. CMS. CERN, Geneva, 1997. https://cds.cern.ch/record/ 343814. [55] CMS Collaboration. Particle-flow reconstruction and global event description with the CMS detector. Journal of Instrumentation, 12(10):P10003, 2017. [56] CMS Collaboration. The phase-2 upgrade of the CMS Endcap Calorimeter. Technical report, CERN, Geneva, Nov 2017. https://cds.cern.ch/record/ 2293646. [57] CMS Collaboration. The Phase-2 Upgrade of the CMS Muon Detectors. Techni- cal report, CERN, Geneva, Sep 2017. https://cds.cern.ch/record/2283189. [58] CMS Collaboration. The Phase-2 Upgrade of the CMS L1 Trigger Interim Technical Design Report. Technical report, CERN, Geneva, Sep 2017. https: //cds.cern.ch/record/2283192. [59] CMS Collaboration. Observation of the diphoton decay of the higgs boson and measurement of its properties. The European Physical Journal C, 74(10). [60] CMS Collaboration. Search for narrow resonances in dilepton mass spectra in proton-proton collisions at  $\sqrt{s}$  = 13 TeV and combination with 8 tev data. Physics Letters B, 768. [61] CMS Collaboration. Measurement of the ZZ production cross section and  $Z \rightarrow l+l-l'+l'-b$  ranching fraction in pp collisions at  $\sqrt{s}$  = 13tev. Physics Letters B, 763:280–303, 2016. [62] CMS Collaboration. Performance of electron reconstruction and selection with the CMS detector in proton-proton collisions at  $\sqrt{s}$  = 8 TeV. JINST, 10(06):P06005, 2015. doi:10.1088/1748-0221/10/06/P06005. [63] CMS Collaboration. Performance of photon reconstruction and identification with the CMS detector in proton-proton collisions at √s= 8 TeV. Jour- nal of Instrumentation, 10(08):P08010-P08010, aug 2015. doi:10.1088/1748-0221/10/08/p08010. [64] CMS collaboration. Electron and photon reconstruction and identification with the CMS experiment at the CERN LHC. JINST, 16(05):P05014, 2021. doi:10.1088/1748-0221/16/05/P05014. [65] CMS Collaboration. Reconstruction of signal amplitudes in the CMS electro- magnetic calorimeter in the presence of overlapping proton-proton interactions. JINST, 15(10):P10002, 2020. doi:10.1088/1748-0221/15/10/P10002. [66] CMS collaboration. Laser monitoring system for the CMS lead tungstate crystal calorimeter. Technical report, CERN, Geneva, Nov 2007. https://cds.cern.ch/record/1073694. [67] CMS collaboration. Energy resolution of the barrel of the CMS electromagnetic calorimeter. Journal of Instrumentation, 2(04):P04004, 2007. [68] C. Patrignani et al. Review of Particle Physics. Chin. Phys. C, 40(10):100001, 2016. doi:10.1088/1674-1137/40/10/100001. [69] Fabrice Couderc. Quest for the Higgs boson(s) from D0 to CMS experiments. Habilitation à diriger des recherches, SORBONNE UNIVERSITE, December 2018. [70] R.A.J. Riddle B.L. Roberts and G.T.A. Squier. Measurement of Lorentzian linewidths. Nuclear Instruments and Methods, 130(2):559-563, 1975. [71] T Czosnyka and A Trzcińska. Unified analytical approximation of Gaussian and Voigtian lineshapes. Nuclear Instruments and Methods in Physics Research Section A, 431(3):548-550, 1999. 141 [72] John Joseph Olivero and R. L.

Longbothum. Empirical fits to the voigt line width: A brief review. Journal of Quantitative Spectroscopy & Radiative Trans- fer, 17:233-236, 1977. [73] CMS Collaboration. The Phase-2 Upgrade of the CMS Barrel Calorimeters. Technical report, CERN, Geneva, Sep 2017. https://cds.cern.ch/record/ 2283187. [74] O. Gevin, F. Guilloux, P. Baron, and M. Dejardin. CATIA: APD readout ASIC for CMS phase 2 ECAL electronics upgrade. doi:10.22323/1.370.0001. [75] S. Cometti and G. Mazza. LiTE-DTU: online data selection, compres- sion, and transmission ASIC for the upgraded frontend of the CMS Elec-tromagnetic Calorimeter. In 2019 8th International Conference on Mod- ern Circuits and Systems Technologies (MOCAST), pages 1-4. IEEE, 2019. doi:10.1109/MOCAST.2019.8741539. [76] J. M. Mendez, S. Baron, S. Kulis, and J. Fonseca. New LpGBT-FPGA IP: Simulation model and first implementation. PoS, TWEPP2018:059, 2019. doi:10.22323/1.343.0059. [77] C Soós, S. Détraz, L. Olanterä, C. Sigaud, J. Troska, F. Vasey, and M. Zeiler. Versatile Link PLUS transceiver development. Journal of Instrumentation, 12(03):C03068, 2017. doi:10.1088/1748-0221/12/03/C03068. [78] CMS Collaboration. The Barrel Calorimeter Processor demonstrator board for the Phase II Upgrade of the CMS ECAL Barrel. Technical report, CERN, Geneva, Oct 2018. https://cds.cern.ch/record/2644903". [79] CMS Collaboration. Technical proposal for the Phase-II Upgrade of the CMS Detector. Technical report, Geneva, Jun 2015. https://cds.cern.ch/record/ 2020886. [80] I. W. Stewart, Frank J. Tackmann, J. Thaler, C. K. Vermilion, and T. F. Wilkason. Xcone: N-jettiness as an exclusive cone jet algorithm. Journal of High Energy Physics, 2015(11), Nov 2015. doi:10.1007/jhep11(2015)072. 142 [81] S. Alioli, P. Nason, C. Oleari, and E. Re. A general framework for implementing NLO calculations in shower Monte Carlo programs: the POWHEG BOX. Jour- nal of High Energy Physics, 2010(6), Jun 2010. doi:10.1007/jhep06(2010)043. [82] M. Czakon and A. Mitov. Top++: A program for the calculation of the top-pair cross-section at hadron colliders. Computer Physics Communications, 185(11):2930-2938, Nov 2014. doi:10.1016/j.cpc.2014.06.021. [83] A. Giammanco. Single top quark production at the LHC. Reviews in Physics, 1:1-12, 2016. doi:10.1016/j.revip.2015.12.001. [84] CMS Collaboration. Performance of the CMS muon detector and muon recon- struction with proton-proton collisions at √s=13 TeV. Journal of Instrumenta- tion, 13(06):P06015-P06015, Jun 2018. doi:10.1088/1748-0221/13/06/P06015. [85] CMS Collaboration. Measurement of the inelastic proton-proton cross sec- tion at  $\sqrt{s}$  = 13 TeV. Journal of High Energy Physics, 2018(7), Jul 2018. doi:10.1007/jhep07(2018)161. [86] A. Bodek, A. Van Dyne, J. Y. Han, W. Sakumoto, and A. Strelnikov. Extract-ing muon momentum scale corrections for hadron collider experiments. The European Physical Journal C, 72(10):1-7, 2012. doi:10.1140/epjc/s10052-012-2194-8. [87] CMS Collaboration. Performance of CMS muon reconstruction in pp collision events at  $\sqrt{s}$  7 TeV. Journal of Instrumentation, 7(10):P10002-P10002, Oct 2012. doi:10.1088/1748-0221/7/10/p10002. [88] S. Schmitt. Tunfold, an algorithm for correcting migration effects in high en- ergy physics. Journal of Instrumentation, 7(10):T10003-T10003, Oct 2012. doi:10.1088/1748-0221/7/10/t10003. [89] N. Tihonov, A. Solution of incorrectly formulated problems and the regular- ization method. Soviet Math., 4:1035-1038, 1963. 143 [90] CMS Collaboration. CMS luminosity measurement for the 2018 data-taking period at  $\sqrt{s}$  =13tev. Technical report, CERN, Geneva, 2019. https://cds. cern.ch/record/2676164. [91] Tracking POG results for pion efficiency with the D\* meson using data from 2016 and 2017. Aug 2018. http://cds.cern.ch/record/2634940. [92] CMS Collaboration. Cms tracking pog performance plots for 2018 dataset. https://twiki.cern.ch/twiki/bin/view/CMSPublic/ TrackingPOGResults2018. [93] S. Alioli, C. W. Bauer, C. Berggren, F. J. Tackmann, and J. R. Walsh. Drell- Yan production at NNLL+NNLO matched to parton showers. Physical Review D, 92(9), Nov 2015. doi:10.1103/physrevd.92.094020. [94] M. Cacciari, G. P. Salam, and G. Soyez. The anti-kt jet clustering algorithm. Journal of High Energy Physics, 2008(04):063-063, Apr 2008. doi:10.1088/1126-6708/2008/04/063. [95] D. Bertolini, P. Harris, M. Low, and N. Tran. Pileup per parti- cle identification. Journal of High Energy Physics, 2014(10):1-22, 2014. doi:10.1007/JHEP10(2014)059. 2 3 4 5 6 7 8 9 10 11 13 14 15 16 17 18 19 20 21

23 24 25 26 27 28 29 30 31 32 33 34 35 36 37 38 39 40 42 43 44 45 46 47 48 49 50 51 52 53 54 55 56 57 58 60 61 66 67 68 69 71 72 73 74 75 76 77 78 81 83 84 85 86 87 89 90 91 92 93 94 95 96 97 98 99 101 102 103 107 109 110 function of one-jettiness for 12 < pT (Z) < 25 GeV. 111 112 function of one-jettiness for 125 < MII < 150 GeV. 113 114 115 116 117 118 119 120 121 122 123 124 125 126 127 128 129 131 132 133 134 136 137 138 139 140 144

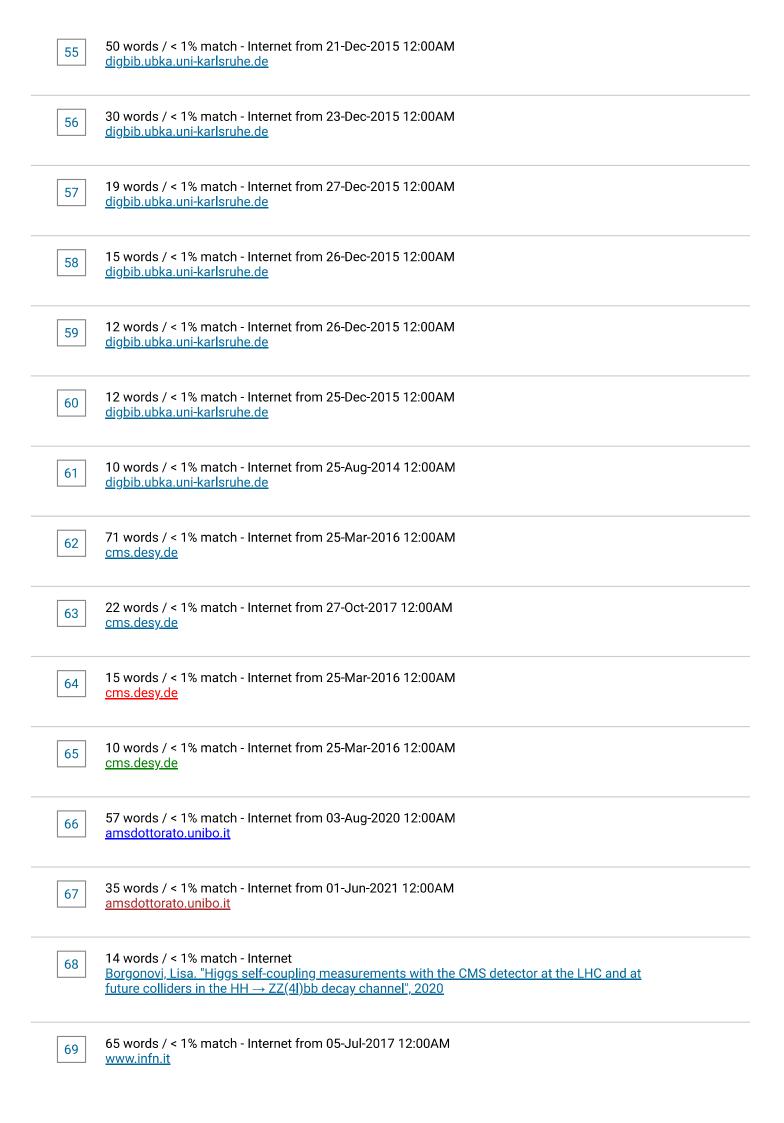
sources:	
1	253 words / 1% - Internet from 25-Apr-2019 12:00AM tel.archives-ouvertes.fr
2	224 words / 1% - Internet from 30-Apr-2019 12:00AM tel.archives-ouvertes.fr
3	305 words / 1% - Internet from 04-May-2021 12:00AM iihe.ac.be
4	311 words / 1% - Crossref  Jelena Mijuskovic. "The CMS electromagnetic calorimeter upgrade: high-rate readout with precise time and energy resolution", Journal of Instrumentation, 2022
5	161 words / 1% - Internet <u>Bierwagen, Katharina. "Physics with Jets in Association with a Z Boson in pp-collisions with the ATLAS Detector at the Large Hadron Collider", 2013</u>
6	108 words / < 1% match - Internet from 14-Apr-2018 12:00AM tel.archives-ouvertes.fr
7	27 words / < 1% match - Internet from 02-Sep-2018 12:00AM tel.archives-ouvertes.fr
8	14 words / < 1% match - Internet from 22-Jul-2020 12:00AM tel.archives-ouvertes.fr
9	12 words / < 1% match - Internet from 05-Dec-2018 12:00AM tel.archives-ouvertes.fr
10	12 words / < 1% match - Internet from 02-May-2019 12:00AM tel.archives-ouvertes.fr
11	10 words / < 1% match - Internet from 10-Apr-2018 12:00AM tel.archives-ouvertes.fr
12	81 words / < 1% match - Internet from 11-Dec-2021 12:00AM d-nb.info



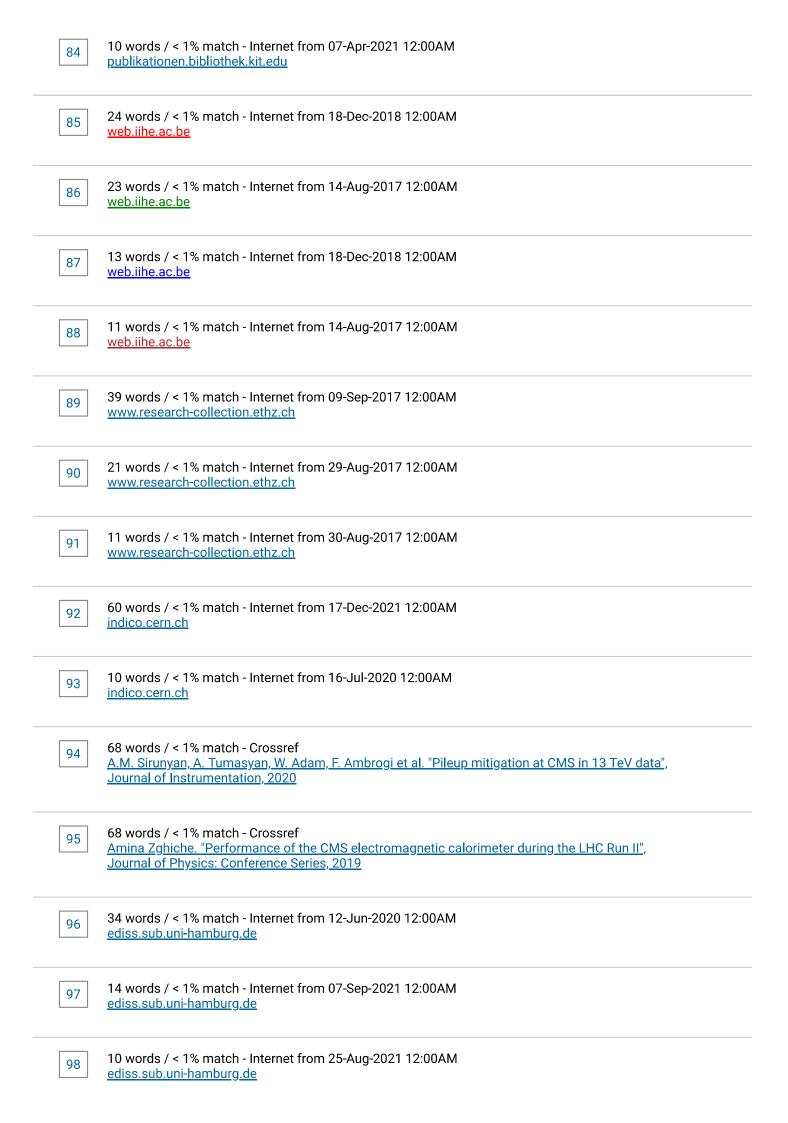
28	10 words / < 1% match - Internet from 03-Oct-2020 12:00AM d-nb.info
29	21 words / < 1% match - Internet from 04-May-2021 12:00AM <u>iihe.ac.be</u>
30	13 words / < 1% match - Internet from 24-Mar-2012 12:00AM <u>iihe.ac.be</u>
31	11 words / < 1% match - Internet from 04-May-2021 12:00AM <u>iihe.ac.be</u>
32	10 words / < 1% match - Internet from 08-Jun-2021 12:00AM <u>iihe.ac.be</u>
33	70 words / < 1% match - Internet  Massironi, Andrea. "Precision electromagnetic calorimetry at the energy frontier: CMS ECAL at  LHC Run 2", 2015
34	38 words / < 1% match - Internet from 18-Jul-2020 12:00AM arxiv.org
35	34 words / < 1% match - Internet from 09-May-2014 12:00AM arxiv.org
36	26 words / < 1% match - Internet  CMS Collaboration. "Energy calibration and resolution of the CMS electromagnetic calorimeter in pp collisions at sqrt(s) = 7 TeV", 2013
37	24 words / < 1% match - Internet from 13-May-2018 12:00AM arxiv.org
38	17 words / < 1% match - Internet from 08-Apr-2021 12:00AM arxiv.org
39	15 words / < 1% match - Internet from 06-Feb-2019 12:00AM arxiv.org
40	11 words / < 1% match - Internet from 21-Dec-2021 12:00AM arxiv.org
41	11 words / < 1% match - Internet from 02-Apr-2020 12:00AM arxiv.org
42	10 words / < 1% match - Internet

## <u>U. De Sanctis, F. Ragusa, A. Andreazza, G. Vegni et al. "Expected Performance of the ATLAS Experiment: Detector, Trigger and Physics", Cern, 2008</u>

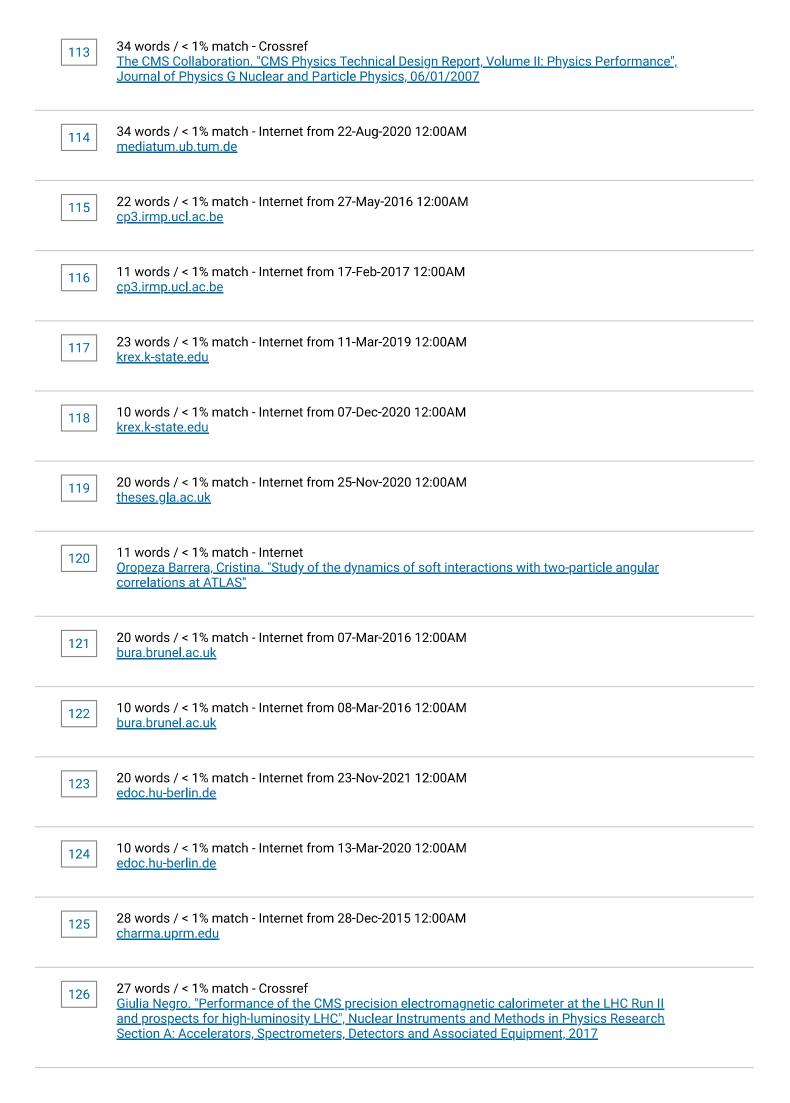
10 words / < 1% match - Internet from 06-Apr-2021 12:00AM 43 arxiv.org 22 words / < 1% match - Internet 44 Ceard, Ludivine. "First measurement of the associated production of a Z boson with b jets at the LHC", 2015 20 words / < 1% match - Internet 45 Torre Pérez, Héctor de la. "Measurement of photon plus jets production and identification of boosted top quarks in pp collisions at the LHC using the ATLAS detector", 2016 15 words / < 1% match - Internet 46 Gude, Alexander. "Measurement of the phistar distribution of Z bosons decaying to electron pairs with the CMS experiment at a center-of-mass energy of 8 TeV", 2015 12 words / < 1% match - Internet 47 Rosien, Nils-Arne. "Measurement of the ttZ Production Cross Section in the Final State with Three Charged Leptons using 36.1 fb^-1 of pp Collisions at 13 TeV at the ATLAS Detector", 2018 11 words / < 1% match - Internet 48 Cantero García, Josu. "A study of the dynamics of isolated-photon plus jet production in pp. collisions at  $\sqrt{8}$ = 7 TeV with the ATLAS detector", 2013 11 words / < 1% match - Internet 49 Wardrope, David Robert, Wardrope, David Robert. "Preparations for measurement of electroweak vector boson production cross-sections using the electron decay modes, with the Compact Muon Solenoid detector", Physics, 2010 10 words / < 1% match - Internet 50 Heikkilä, Jaana. "Search for a Pseudoscalar Higgs boson in the Context of Two-Higgs-Doublet Models", 'University of Helsinki Libraries', 2019 101 words / < 1% match - Internet from 08-Sep-2019 12:00AM 51 boa.unimib.it 57 words / < 1% match - Internet from 12-Apr-2016 12:00AM 52 boa.unimib.it 26 words / < 1% match - Internet from 08-Dec-2017 12:00AM 53 boa.unimib.it 23 words / < 1% match - Internet from 12-Apr-2016 12:00AM 54 boa.unimib.it

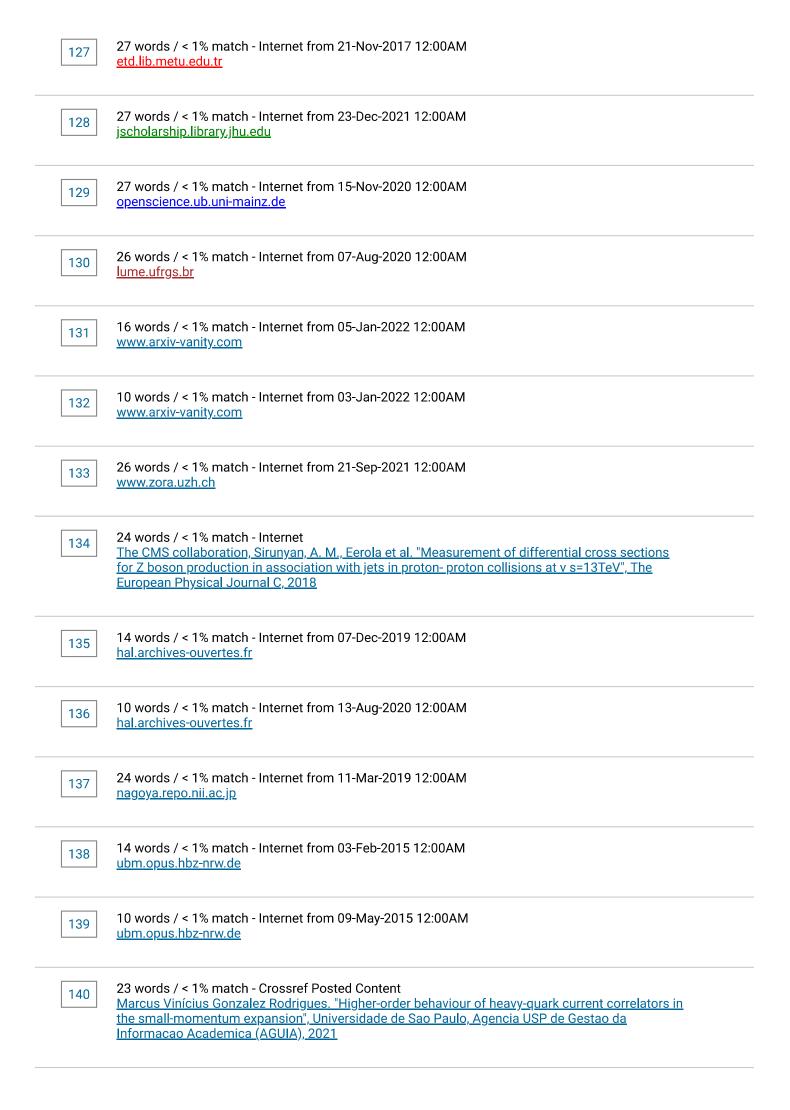


70	12 words / < 1% match - Internet from 04-Feb-2017 12:00AM www.infn.it
71	11 words / < 1% match - Internet from 04-Feb-2017 12:00AM www.infn.it
72	46 words / < 1% match - Internet from 27-Dec-2021 12:00AM dipot.ulb.ac.be
73	33 words / < 1% match - Internet from 15-Apr-2021 12:00AM dipot.ulb.ac.be
74	33 words / < 1% match - Internet from 10-Mar-2020 12:00AM worldwidescience.org
75	17 words / < 1% match - Internet from 29-Jul-2020 12:00AM worldwidescience.org
76	17 words / < 1% match - Internet from 24-Dec-2010 12:00AM worldwidescience.org
77	12 words / < 1% match - Internet from 01-Aug-2020 12:00AM worldwidescience.org
78	53 words / < 1% match - Internet from 28-May-2016 12:00AM etd.adm.unipi.it
79	22 words / < 1% match - Internet from 29-May-2016 12:00AM etd.adm.unipi.it
80	22 words / < 1% match - Internet from 17-Nov-2020 12:00AM publikationen.bibliothek.kit.edu
81	21 words / < 1% match - Internet from 12-Nov-2020 12:00AM publikationen.bibliothek.kit.edu
82	11 words / < 1% match - Internet <u>Berger, Thomas. "Jet energy calibration and triple differential inclusive cross section</u> <u>measurements with Z (<math>\rightarrow \mu \mu</math>) + jet events at 13 TeV recorded by the CMS detector", KIT-Bibliothek, Karlsruhe, 2019</u>
83	10 words / < 1% match - Internet from 22-May-2021 12:00AM publikationen.bibliothek.kit.edu

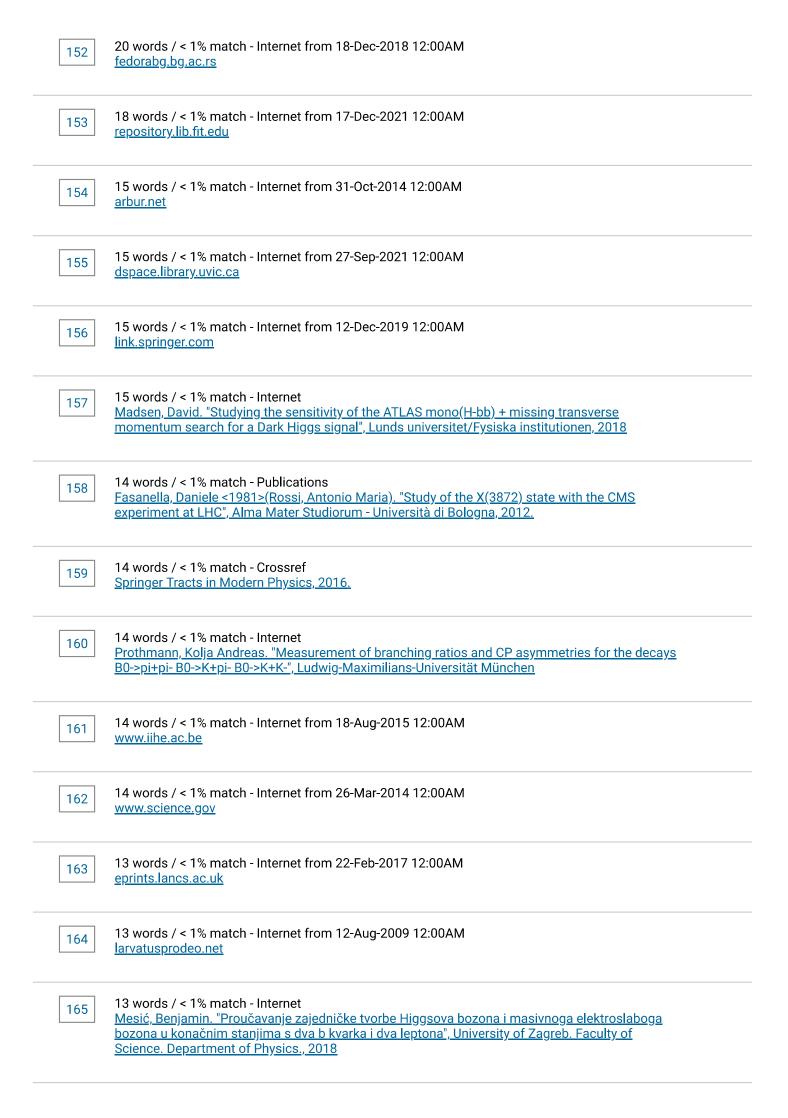


23 words / < 1% match - Internet from 23-Jan-2019 12:00AM pastel.archives-ouvertes.fr
21 words / < 1% match - Internet from 10-Nov-2018 12:00AM pastel.archives-ouvertes.fr
101 11 words / < 1% match - Internet from 17-Apr-2019 12:00AM pastel.archives-ouvertes.fr
26 words / < 1% match - Internet from 24-Aug-2014 12:00AM www.freidok.uni-freiburg.de
23 words / < 1% match - Internet from 25-Aug-2014 12:00AM www.freidok.uni-freiburg.de
23 words / < 1% match - Internet from 17-Dec-2018 12:00AM thesis.library.caltech.edu
11 words / < 1% match - Internet from 30-Nov-2018 12:00AM thesis.library.caltech.edu
10 words / < 1% match - Internet from 10-Oct-2019 12:00AM thesis.library.caltech.edu
30 words / < 1% match - Internet from 28-Aug-2019 12:00AM fulir.irb.hr
10 words / < 1% match - Internet from 09-Feb-2021 12:00AM fulir.irb.hr
38 words / < 1% match - Internet from 23-Apr-2016 12:00AM pos.sissa.it
25 words / < 1% match - Internet from 05-Apr-2021 12:00AM escholarship.org
111 words / < 1% match - Internet from 10-Oct-2021 12:00AM escholarship.org
34 words / < 1% match - Crossref  A. Tumasyan, W. Adam, J. W. Andrejkovic, T. Bergauer et al. "Study of Z boson plus jets events using variables sensitive to double-parton scattering in pp collisions at 13 TeV", Journal of High Energy Physics, 2021





- 12 words / < 1% match Internet from 12-May-2021 12:00AM 141 tud.qucosa.de 11 words / < 1% match - Internet from 29-Apr-2019 12:00AM 142 tud.qucosa.de 22 words / < 1% match - Publications 143 Abadjiev, K, Abbaneo, D, Abbiendi, G, Abbrescia, M, Abdullin, S, Abelev, B, Acosta, D, Acosta, JG, Acosta, MV, Actis, O, Adam, N, Adam, W, Adams, MR, Adams, T, Adiguzel, A, Adler, V, Adolphi, R, Adzic, P, Afaq, MA, Agostino, L, Agram, JL, Aguilar-Benitez, M, Ahmad, M, Ahmad, WH, Ahmed, I, Ahmed, W, Ahuja, S, Aisa, D, Aisa, S, Akchurin, N, Akgun, B, Akgun, U, Akimenko, S, Akin, IV, Alagoz, E, Alampi, G, Albajar, C, Albayrak, EA, Alberdi, J, Albergo, S, Albert, E, Albrow, M, Alexander, J, Alidra, M, Aliev, T, Allfrey, P, Almeida, N, Altenhofer, G, Altsybeev, I, Alver, B, Alverson, G, Alves, GA, Amaglobeli, N, Amapane, N, Ambroglini, F, Amsler, C, Anagnostou, G, Ananthan, B, Anastassov, A, Andelin, D, Anderson, M, Andrea, J, Andreev, V, Andreev, Y, Anghel, IM, Anguelov, T, Anisimov, A, Antillon, E, Antipov, P, Antonelli, L, Anttila, E, Antunes, JR, Antunovic, Z, Apanasevich, L, Apollinari, G, Apresyan, A, Arce, P, Arcidiacono, R, Arenton, MW, Arfaei, H, Argiro, S, Arisaka, K, Arneodo, M et al. "Commissioning of the CMS experiment and the cosmic run at four tesla", Institute of Physics, 2012. 22 words / < 1% match - Publications 144 Chadwick, Matthew(Hobson, PR and Khan, A). "Measurement of the t(t^-) cross-section at 7 TeV with 36 PB-1 of data in the electron+jets decay channel using the CMS detector", Brunel University School of Engineering and Design PhD Theses, 2012. 12 words / < 1% match - Internet 145 MORGAN, THOMAS, ANTHONY. "Precision Z Boson Phenomenology at the LHC", 2016 10 words / < 1% match - Internet from 24-Nov-2020 12:00AM 146 etheses.dur.ac.uk 22 words / < 1% match - Internet from 24-Apr-2016 12:00AM 147 media.proquest.com 11 words / < 1% match - Internet 148 Zucchetta, Alberto. "Searches for signatures of an extended Higgs sector in final states with leptons and Higgs to bb decays at CMS", 2015 10 words / < 1% match - Internet from 16-Nov-2018 12:00AM 149 paduaresearch.cab.unipd.it 21 words / < 1% match - Internet 150 Sudić, Lucija. "Proučavanje zajedničke tvorbe bozona W i Z detektorom CMS u sudarima protona i protona na Velikom hadronskom sudarivaču", University of Zagreb. Faculty of Science. Department of Physics.
  - 20 words / < 1% match Crossref
    R. Yohay. "The CMS High Granularity Calorimeter for High Luminosity LHC", Nuclear Instruments
    and Methods in Physics Research Section A: Accelerators, Spectrometers, Detectors and
    Associated Equipment, 2020



13 words / < 1% match - Internet from 21-Jul-2020 12:00AM 166 web.physik.rwth-aachen.de 12 words / < 1% match - Crossref 167 A. M. Sirunyan, A. Tumasyan, W. Adam, J. W. Andrejkovic et al. " Search for lepton-flavor violating decays of the Higgs boson in the and final states in proton-proton collisions at ", Physical Review D, 2021 12 words / < 1% match - Publications 168 Scheidle, Thorsten. "Spurrekonstruktion in Vorwärtsrichtung mit dem Silizium-Vertexdetektor des CDF-Experiments in RUN II. Forward tracking with the silicon vertex detector at the CDF experiment in RUN II", Universität Karlsruhe, 2007. 12 words / < 1% match - Publications 169 Schmidt, Evelyn. "Search for the Standard Model Higgs boson in the \$H rightarrow W^{+}W^{-} rightarrow ell^{+} nu ell^{-} bar{nu}\$ decay mode in proton-proton collisions at \${sqrt{s}=7\$ TeV and \$sqrt(s)=8\$ TeV with the ATLAS experiment", Universität Freiburg, 2013. 12 words / < 1% match - Crossref 170 Springer Theses, 2015. 12 words / < 1% match - Crossref 171 Thorben Quast. "Chapter 2 Particle Physics at the Large Hadron Collider", Springer Science and Business Media LLC, 2021 12 words / < 1% match - Crossref 172 <u>Ulascan Sarica. "Measurements of Higgs Boson Properties in Proton-Proton Collisions at √s =7, 8</u> and 13 TeV at the CERN Large Hadron Collider", Springer Science and Business Media LLC, 2019 12 words / < 1% match - Internet from 25-Jan-2022 12:00AM 173 confluence.desy.de 12 words / < 1% match - Internet from 02-Jan-2022 12:00AM 174 core.ac.uk 12 words / < 1% match - Internet from 07-Dec-2014 12:00AM 175 edoc.ub.uni-muenchen.de 12 words / < 1% match - Internet from 18-Nov-2021 12:00AM 176 <u>ujcontent.uj.ac.za</u> 11 words / < 1% match - Crossref 177 Checchia, Paolo. "Implications of a 125 GeV Higgs boson", International Journal of Modern Physics A, 2015. 11 words / < 1% match - Crossref 178 lain W. Stewart, Frank J. Tackmann, Wouter J. Waalewijn. "Jettiness: An Inclusive Event Shape to Veto Jets ", Physical Review Letters, 2010

179 11 words / < 1% match - Crossref

L. Brianza. "Precision crystal calorimetry in LHC Run II with the CMS ECAL", Journal of Instrumentation, 2017

11 words / < 1% match - Crossref

<u>Simone Alioli, Alessandro Broggio, Matthew A. Lim. "Zero-jettiness resummation for top-quark pair production at the LHC", Journal of High Energy Physics, 2022</u>

- 11 words / < 1% match Internet from 21-Sep-2021 12:00AM biblio.ugent.be
- 11 words / < 1% match Internet from 04-Nov-2021 12:00AM dspace.mit.edu
- 11 words / < 1% match Internet from 28-Jan-2022 12:00AM libratez.cu.edu.tr
- 11 words / < 1% match Internet
  Schizzi, Andrea. "Associated production of W bosons and two jets from b quarksat the CMS
  experiment.", Università degli studi di Trieste, 2015
- 10 words / < 1% match Crossref

  A. Quadt. "Top quark physics at hadron colliders", The European Physical Journal C, 2006
- 10 words / < 1% match Crossref

  A. Tumasyan, W. Adam, J. W. Andrejkovic, T. Bergauer et al. "Measurement of double-parton scattering in inclusive production of four jets with low transverse momentum in proton-proton collisions at \$\$ \sqrt \$\$ = 13 TeV", Journal of High Energy Physics, 2022
- 10 words / < 1% match Crossref

  A.M. Sirunyan, A. Tumasyan, W. Adam, T. Bergauer et al. "Electron and photon reconstruction and identification with the CMS experiment at the CERN LHC", Journal of Instrumentation, 2021
- 10 words / < 1% match Crossref
  Bevan, A. J., B. Golob, Th. Mannel, S. Prell, B. D. Yabsley, H. Aihara, F. Anulli, N. Arnaud, T. Aushev,
  M. Beneke, J. Beringer, F. Bianchi, I. I. Bigi, M. Bona, N. Brambilla, J. Brodzicka, P. Chang, M. J.
  Charles, C. H. Cheng, H.-Y. Cheng, R. Chistov, P. Colangelo, J. P. Coleman, A. Drutskoy, V. P.
  Druzhinin, S. Eidelman, G. Eigen, A. M. Eisner, R. Faccini, K. T. Flood, P. Gambino, A. Gaz, W. Gradl,
  H. Hayashii, T. Higuchi, W. D. Hulsbergen, T. Hurth, T. Iijima, R. Itoh, P. D. Jackson, R. Kass, Yu. G.
  Kolomensky, E. Kou, P. Križan, A. Kronfeld, S. Kumano, Y. J. Kwon, T. E. Latham, D. W. G. S. Leith, V.
  Lüth, F. Martinez-Vidal, B. T. Meadows, R. Mussa, M. Nakao, S. Nishida, J. Ocariz, S. L. Olsen, P.
  Pakhlov, G. Pakhlova, A. Palano, A. Pich, S. Playfer, A. Poluektov, F. C. Porter, S. H. Robertson, J. M.
  Roney, A. Roodman, Y. Sakai, C. Schwanda, A. J. Schwartz, R. Seidl, S. J. Sekula, M. Steinhauser, K.
  Sumisawa, E. S. Swanson, F. Tackmann, K. Trabelsi, S. Uehara, S. Uno, R. van de Water, G. Vasseur
  et al. "The Physics of the B Factories", The European Physical Journal C, 2014.

10 words / < 1% match - Crossref
Biagio Di Micco, Maxime Gouzevitch, Javier Mazzitelli, Caterina Vernieri. "Higgs boson potential at colliders: Status and perspectives", Reviews in Physics, 2020

190	10 words / < 1% match - Publications <u>Karstens, Falk. "Charm Production in Deep Inelastic Scattering at the ZEUS Experiment in the HERA-II data period", Universität Freiburg, 2006.</u>
191	10 words / < 1% match - Publications Niegel, Martin. "Search for Supersymmetry in Trimuon Final States with the CMS Detector", Universität Karlsruhe, 2009.
192	10 words / < 1% match - Publications University of Tennessee, Knoxville
193	10 words / < 1% match - Crossref <u>Wan-Li Ju, Marek Schönherr. "The qT and Δφ spectra in W and Z production at the LHC at N3LL'</u> +N2LO", Journal of High Energy Physics, 2021
194	10 words / < 1% match - Internet from 15-May-2018 12:00AM authors.library.caltech.edu
195	10 words / < 1% match - Internet from 09-Apr-2019 12:00AM elpub.bib.uni-wuppertal.de
196	10 words / < 1% match - Internet from 23-Mar-2019 12:00AM export.arxiv.org
197	10 words / < 1% match - Internet from 29-Aug-2017 12:00AM fisica.mib.infn.it
198	10 words / < 1% match - Internet from 05-Nov-2017 12:00AM freidok.uni-freiburg.de
199	10 words / < 1% match - Internet from 18-Oct-2010 12:00AM heim.ifi.uio.no
200	10 words / < 1% match - Internet from 06-Dec-2017 12:00AM jyx.jyu.fi
201	10 words / < 1% match - Internet from 11-Dec-2021 12:00AM livrepository.liverpool.ac.uk
202	10 words / < 1% match - Internet from 10-Aug-2020 12:00AM mafiadoc.com
203	10 words / < 1% match - Internet from 18-Jul-2019 12:00AM pure.uva.nl

1 / 114 1	ords / < 1% match - Internet from 25-Mar-2019 12:00AM sitorio.uam.es
	ords / < 1% match - Internet from 29-Apr-2021 12:00AM sitorio.unican.es
	ords / < 1% match - Internet from 23-Mar-2021 12:00AM lar.smu.edu
	ords / < 1% match - Internet from 09-Jan-2022 12:00AM  arworks.bwise.kr
1 / 1 / 1	ords / < 1% match - Internet oldi, Fabio. "Study of B → μ+μ- decays with the ATLAS detector", 2020
	ords / < 1% match - Internet from 08-Sep-2017 12:00AM cab.unipd.it
1 / 10 1	ords / < 1% match - Internet from 10-Jul-2021 12:00AM .fedoa.unina.it
1 / 1 1 1	ords / < 1% match - Internet from 11-Jan-2022 12:00AM <u>hepdata.net</u>
1 / 1 / 1	ords / < 1% match - Internet from 05-Jan-2022 12:00AM .pure.ed.ac.uk
1 / 1.5 1	ords / < 1% match - Internet from 05-Feb-2017 12:00AM .roma1.infn.it